

FAST RADIO BURSTS AS A PROBE OF GRAVITY ON COSMOLOGICAL SCALES

DENNIS NEUMANN

Leiden Observatory, Leiden University, P.O. Box 9513, 2300 RA Leiden, the Netherlands and
Ruhr University Bochum, Faculty of Physics and Astronomy, Astronomical Institute (AIRUB), German Centre for Cosmological
Lensing, 44780 Bochum, Germany

ROBERT REISCHKE

Argelander-Institut für Astronomie, Universität Bonn, Auf dem Hügel 71, D-53121 Bonn, Germany and
Ruhr University Bochum, Faculty of Physics and Astronomy, Astronomical Institute (AIRUB), German Centre for Cosmological
Lensing, 44780 Bochum, Germany

STEFFEN HAGSTOTZ

Universitäts-Sternwarte, Fakultät für Physik, Ludwig-Maximilians Universität München, Scheinerstraße 1, D-81679 München,
Germany and
Excellence Cluster ORIGINS, Boltzmannstraße 2, D-85748 Garching, Germany

HENDRIK HILDEBRANDT

Ruhr University Bochum, Faculty of Physics and Astronomy, Astronomical Institute (AIRUB), German Centre for Cosmological
Lensing, 44780 Bochum, Germany
Version June 17, 2025

ABSTRACT

We explore the potential for improving constraints on gravity by leveraging correlations in the dispersion measure derived from Fast Radio Bursts (FRBs) in combination with cosmic shear. Specifically, we focus on Horndeski gravity, inferring the kinetic braiding and Planck mass run rate from a stage-4 cosmic shear mock survey alongside a survey comprising 10^4 FRBs. For the inference pipeline, we utilise the Boltzmann code `hi_class` to predict the linear matter power spectrum in modified gravity scenarios, while non-linear corrections are obtained from the halo-model employed in `HMcode`, including feedback mechanisms. Our findings indicate that FRBs can disentangle degeneracies between baryonic feedback and cosmological parameters, as well as the mass of massive neutrinos. Since these parameters are also degenerate with modified gravity parameters, the inclusion of FRBs can enhance constraints on Horndeski parameters by up to 40 percent, despite being a less significant measurement. Additionally, we apply our model to current FRB data and use the uncertainty in the $DM - z$ relation to impose limits on gravity. However, due to the limited sample size of current data, constraints are predominantly influenced by theoretical priors. Despite this, our study demonstrates that FRBs will significantly augment the limited set of cosmological probes available, playing a critical role in providing alternative tests of feedback, cosmology, and gravity. All codes used in this work are made publicly available.

Keywords: Cosmology, Fast Radio Bursts, Modified Gravity, Horndeski

1. INTRODUCTION

The Universe entered a phase of accelerated expansion around four billion years ago (Riess et al. 1998). This effect is one of the greatest unsolved mysteries of modern cosmology and understanding the mechanisms behind this *dark energy* is the proclaimed science goal of the stage-4 cosmological surveys Euclid¹, Rubin-LSST² and the Roman telescope³. In the standard model of cosmology, dark energy is viewed as a perfect fluid driven by the cosmological constant Λ . Even though this picture is well motivated at the moment (Tripathi et al. 2017; Planck Collaboration et al. 2020b; Escamilla et al. 2024), accurate modelling of the dark energy dynamics is of utmost importance due to its implication of large-scale

structure (LSS) formation. The recent DESI findings of a possibly time-dependent dark energy equation of state (DESI Collaboration et al. 2025) further compel us to explore alternative gravity models. The simplest modifications to GR involve a dynamic dark energy fluid driven by an additional scalar degree of freedom in the relativistic field equations. A plethora of these modifications are being actively investigated on the cosmological level, including but not limited to *Quintessence* (Ratra 1988), *Chameleon* (Khoury & Weltman 2004a) and *f(R)* (Carroll et al. 2004). Such theories, including GR, can be generalised under *Horndeski theory* (Horndeski 1974); the most general scalar-tensor theory that has second-order field equations (Kobayashi 2019).

Even though GR is an excellent description of gravity on small cosmic scales, small deviations on larger scales have not been ruled out, yet (Alonso et al. 2017; Heisenberg 2019; Reischke et al. 2019; Spurio Mancini et al. 2018a, 2019). Furthermore, differences in LSS

*dneumann@strw.leidenuniv.nl

†reischke@posteo.net

¹ <https://www.euclid-ec.org/>

² <https://www.lsst.org/>

³ <https://roman.gsfc.nasa.gov/>

between individual theories can be marginal, necessitating the development of precise cosmological tools. The aforementioned stage-4 surveys will map billions of galaxies which will subsequently be used for inferring cosmic evolution by means of statistical weak gravitational lensing (WL) analyses, amongst others (see e.g. Weinberg et al. 2013).

While WL is a particularly strong probe for the underlying matter distribution and its “clumpiness” specifically (Secco et al. 2022), current and future surveys are limited by uncertainties of baryonic processes (Tröster et al. 2022). This problem will only become more severe with more resolved data and hence lower noise levels unveiling correlations on scales smaller than 1Mpc, where baryonic feedback can suppress the power spectrum by up to 40% (Chisari et al. 2019a). In particular, the general shape of this suppression is unknown, thus, requiring tight priors in order to be used in cosmological inference. A solution might be the steady rise of Fast Radio Burst (FRB) measurements (Lorimer et al. 2007; CHIME/FRB Collaboration et al. 2021); broad, millisecond transient pulses in the radio frequency range that get dispersed by free electrons along their line of sight and that are consequently highly sensitive to baryons. Even though their origin is still debated (Petroff et al. 2019), the majority of them must be of extragalactic origin due to their high Dispersion Measure (DM). Naturally, they have been proposed as a LSS probe (Zhou et al. 2014), in particular since the Signal-to-Noise Ratio (SNR) of individual measurements is already ample (Yang & Zhang 2016). FRBs are versatile; they have been suggested as a tool to find the missing baryon content in the intergalactic medium (Muñoz & Loeb 2018), or more generally as an $\Omega_b h^2$ probe (Walters et al. 2018). Furthermore, investigating modified gravity with them is not a new concept. Their low-resolution high-SNR nature was utilised in strong gravitational fields before (Adi & Kovetz 2021, Jiang et al. 2024) but the lack of host-identified FRBs prevents a statistically meaningful LSS analysis in the WL regime. The Square Kilometre Array (SKA⁴, Dewdney et al. 2009) will address this problem at the latest (Hashimoto et al. 2020). Until then, we need to identify the expected constraining power and, in particular, limitations of the currently available modelling tools. So far, investigations focused on how to leverage the averaged cosmological signal, the so-called DM – z relation (e.g. Zhou et al. 2014; Walters et al. 2018; Hagstotz et al. 2022; Macquart et al. 2020; Wu et al. 2022; James et al. 2022; Reischke & Hagstotz 2023a,b) or the statistics of DM fluctuations (e.g. Masui & Sigurdson 2015; Shirasaki et al. 2017; Rafiei-Ravandi et al. 2021; Bhattacharya et al. 2021; Takahashi et al. 2021; Reischke et al. 2021, 2022, 2023) to constrain the cosmological standard model.

In this work, we extend the previous work shown in Reischke et al. (2023) and forecast the constraining power arising from a joint FRB+WL measurement on a broad selection of cosmological parameters, in particular those describing perturbations to GR in the form of Horndeski theory. We aim to quantify the improvement in precision when combining a virtual FRB survey feasible within the next decade with stage-4 data, as well as identify shortcomings of the currently available numerical modelling. In Section 2 we first introduce Horndeski theory while focusing on its parameterisation implemented by the `hi_class`⁵ (Zumalacárregui et al.

2017) suite we are using. Afterwards, we lay out the angular power spectrum signal and noise for WL and FRB auto- and cross-correlation in modified gravity. Then, in Section 3, we specify the mock catalogues used in this work. Afterwards, we explain how we obtain the likelihood based on emulated cosmological functions, namely the three-dimensional electron and matter power spectrum and the modified gravity change to the Poisson equation and line element in conformal Newtonian gauge. Here, we list the full set of fixed and inferred cosmological parameters with their respective fiducial value. With the emulated functions we obtain the likelihood and thus, through nested sampling with an MCMC-algorithm, the results displayed in Section 4. There, we showcase the constraints for a small and a large deviation of gravitational dynamics from GR and explore the influence of our Horndeski theory parameter priors on the overall resulting contours. We argue that, while we see an improvement when cross-correlating FRBs with WL, we experience a loss in accuracy from underlying model limitations that must be considered when analysing real data as it becomes available. In Section 5 we apply the outlined procedure to the covariance of FRBs with host identification. A full summary of the results is found in Section 6.

The code, data and trained emulators used in this work are publicly available via `git` on https://github.com/DennisNeumann97/frb_horndeski_forecast for the forecast and on https://github.com/rreischke/frb_covariance for the LSS covariance of FRBs also described in Reischke & Hagstotz (2023b).

2. THEORY

2.1. Horndeski theory

As opposed to the standard cosmological model, the Lagrangian density in Horndeski modified gravity depends on the metric tensor $g^{\mu\nu}$ and an additional scalar degree of freedom ϕ (Horndeski 1974). It can be written as

$$\mathcal{L}[g_{\mu\nu}, \phi, \psi] = \left(\sum_{n=2}^5 \mathcal{L}_n[g_{\mu\nu}, \phi] + \mathcal{L}_M[g_{\mu\nu}, \psi] \right) \quad (1)$$

and enters the action according to

$$S = \int d^4x \sqrt{-g} \mathcal{L}. \quad (2)$$

$\mathcal{L}_M[g^{\mu\nu}, \psi]$ denotes contribution of the matter field ψ to the Lagrangian density. With the covariant derivative $\phi_{;\mu} := \nabla_\mu \phi$, the d'Alembert operator $\square \phi := g^{\mu\nu} \phi_{;\mu;\nu}$ and the scalar field canonical kinetic energy $X := -g^{\mu\nu} \phi_{;\mu} \phi_{;\nu} / 2$, the \mathcal{L}_n are given by

$$\begin{aligned} \mathcal{L}_2 &= G_2(\phi, X), \\ \mathcal{L}_3 &= -G_3(\phi, X) \square \phi, \\ \mathcal{L}_4 &= G_4(\phi, X) R + G_{4;X}(\phi, X) [(\square \phi)^2 - \phi^{;\mu\nu} \phi_{;\mu\nu}], \\ \mathcal{L}_5 &= G_5(\phi, X) G^{\mu\nu} \phi_{;\mu;\nu} - \frac{1}{6} G_{5;X}(\phi, X) \\ &\quad \times [(\square \phi)^3 - 3 \square \phi \phi^{;\mu\nu} \phi_{;\mu\nu} + 2 \phi_{;\mu}{}^\nu \phi_{;\nu}{}^\lambda \phi_{;\lambda}{}^\mu], \end{aligned} \quad (3)$$

where G_2, G_3, G_4 and G_5 are arbitrary functions of ϕ and X . Bellini & Sawicki (2014) have redefined the G_i into four time-dependent functions α_i that fully describe linear perturbations to the Horndeski action shown in Eq. 2. With the help of the now time dependent Planck

⁴ <https://www.skao.int/>

⁵ http://miguelzuma.github.io/hi_class_public/

mass

$$M_{\text{Pl}}^2 := 2 \left(G_4 + X(G_{5;\phi} - 2G_{4;X} - H\dot{\phi}G_{5;X}) \right)$$

they can be written as:

$$HM_{\text{Pl}}^2 \alpha_{\text{M}} := \frac{d}{dt} M_{\text{Pl}}^2,$$

$$\begin{aligned} HM_{\text{Pl}}^2 \alpha_{\text{K}} := & 2X(G_{2;X} + 2XG_{2;XX} - 2G_{3;\phi} - 2XG_{3;\phi X}) \\ & + 12\dot{\phi}XH(G_{3;X} + X(G_{3;XX} - 2G_{4;\phi XX}) - 3G_{4;\phi X}) \\ & + 12XH^2(G_{4;X} + 8XG_{4;XX} + 4X^2G_{4;XXX}) \\ & + 12XH^2(G_{5;\phi} + 5XG_{5;\phi X} + 2X^2G_{5;\phi XX}) \\ & + 4\dot{\phi}XH^4(3G_{5;X} + 7XG_{5;XX} + 2X^2G_{5;XXX}), \end{aligned}$$

$$\begin{aligned} HM_{\text{Pl}}^2 \alpha_{\text{B}} := & 2\dot{\phi}(XG_{3;X} - G_{4;\phi} - 2XG_{4;\phi X}) \\ & + 8XH(G_{4;X} + 2XG_{4;XX} - G_{5;\phi} - XG_{5;\phi X}) \\ & + 2\dot{\phi}XH^2(3G_{5;X} + 2XG_{5;XX}), \end{aligned}$$

$$M_{\text{Pl}}^2 \alpha_{\text{T}} := 2X \left(2G_{4;X} - 2G_{5;\phi} - (\ddot{\phi} - \dot{\phi}H) G_{5;X} \right), \quad (4)$$

where H denotes the time-dependent Hubble parameter. Physically, these functions can be interpreted as follows (Bellini et al. 2016):

- *Planck-mass run rate* α_{M}

In Horndeski-type theories, the Planck-Mass is not necessarily a constant. Its evolution through cosmic history is captured by α_{M} . A boundary condition is necessary to well-define the Planck mass. A sensible choice is to use the value it possesses today on small scales $M_{\text{Pl}}^{\text{ini}}$. This is a free parameter if a screening mechanism forces Horndeski theory to reduce to GR on small scales. Otherwise, it must be the observed value $M_{\text{Pl}}^{\text{ini}} = 2.176434(24) \cdot 10^{-8} \text{ kg}$ (Tiesinga et al. 2021). $\alpha_{\text{M}} \neq 0$ indicates a non-minimally coupled theory of gravity⁶. In that case, α_{M} creates anisotropic stress.

- *kineticity* α_{K}

This is the “kinetic energy of scalar perturbations arising directly from the action” (Bellini & Sawicki 2014). This parameter is largely unconstrained by the LSS (Spurio Mancini et al. 2019).

- *braiding* α_{B}

This term measures the mixing between the canonical kinetic terms of the scalar field and the metric. It is particularly interesting for the scope of this paper because it modifies the growth of perturbations and the shape of the power spectrum, by causing “clustering” of dark energy (Bellini & Sawicki 2014).

- *tensor speed excess* α_{T}

This parameter quantifies the deviation of the speed of gravitational waves c_{grav} to the speed of light c_{light} . Using multi-messenger astronomy, Abbott et al. (2017) have shown that

$$|1 - c_{\text{grav}}/c_{\text{light}}| < 3 \times 10^{-15} \quad (5)$$

⁶ Meaning the “charge” of gravity (the metric $g_{\mu\nu}$) has a more complicated relationship to the scalar field ϕ than linear scaling.

on scales LIGO (LIGO Scientific Collaboration et al. 2015) is sensitive to. However, the tensor speed excess could be in principle scale dependent due to various screening mechanisms and the implications of this measurement as still debated (De Rham & Melville 2018; Noller 2020). The Laser Interferometer Space Antenna (LISA, Auclair et al. 2023) will likely be sensitive enough to give conclusive measurements of α_{T} on cosmic scales. Nevertheless, we employ the assumption here that $\alpha_{\text{T}} = 0$ for linear perturbations. This rules out a substantial amount of modified gravity theories acting on dark energy. Still, popular theories like quintessence (Ratra & Peebles 1988) and $f(R)$ (Carroll et al. 2004) remain viable (Ezquiaga & Zumalacárregui 2017).

Many previously investigated modified gravity theories can be recovered if these functions take on a specific form (see Bellini et al. (2016) for a non-exhaustive list). Most notably, for $\alpha_{\text{M}} = \alpha_{\text{K}} = \alpha_{\text{B}} = \alpha_{\text{T}} = 0$ the Lagrangian reduces to the one from GR and the standard model of cosmology is retrieved.

In practice, we link the evolution of $\alpha_i(t)$ to the dark energy density $\Omega_{\Lambda}(t)$ via linear scaling coefficients $\hat{\alpha}_i$ according to

$$\alpha_i(t) = \hat{\alpha}_i \Omega_{\Lambda}(t). \quad (6)$$

Well aware that this parameterisation can break down at redshifts $z > 10$ (Linder 2017), a strong motivation for Horndeski theory is whether the late time accelerated expansion of the Universe can (partly) be explained with a non-GR gravity on large cosmic scales. The energy density is driven by the same functions as the α_i , so we could naively expect $\hat{\alpha}_i \sim \mathcal{O}(1)$ (Bellini et al. 2016). Thus, since the kineticity affects LSS evolution only marginally at best, we adapt henceforth $\hat{\alpha}_{\text{K}} = 1$. Considering the constraints on α_{T} , the Horndeski theory cosmological parameters inferred in this work will be the braiding and Planck mass run rate proportionality constants, $\hat{\alpha}_{\text{B}}$ and $\hat{\alpha}_{\text{M}}$, respectively. Note that we do not vary the dark energy equation of state here explicitly since our focus is on the modifications to GR on the perturbation level and not at the background.

Naturally, changing the field equations that determine the metric also affect geodesics, influencing the weak gravitational lensing formalism in particular. We choose conformal Newtonian gauge for the coupling between geodesics and matter fields which is a common choice for scalar perturbation theories (Ma & Bertschinger 1995):

$$ds^2 = a^2(\tau) \left[-c^2 \left(1 + \frac{2\Psi}{c^2} \right) d\tau^2 + \left(1 - \frac{2\Phi}{c^2} \right) d\mathbf{x}^2 \right]. \quad (7)$$

c is the speed of light and Ψ and Φ are the Newtonian perturbative potentials, also known as Bardeen potentials (Bardeen 1980), dependent on the position \mathbf{x} and scale factor a . Following Planck Collaboration et al. (2016), we introduce two phenomenological functions in Fourier space that characterise linear structure formation in modified gravity: The ratio of the Bardeen potentials

$$\eta(\mathbf{k}, a) := \frac{\tilde{\Phi}(\mathbf{k}, a)}{\tilde{\Psi}(\mathbf{k}, a)} \quad (8)$$

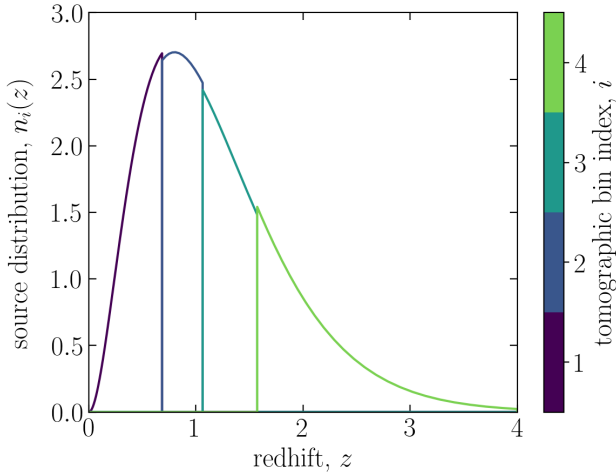


Figure 1. Tomographic source redshift distribution of the mock FRB catalogue. The discontinuities between bins originate from normalising each source distribution individually.

and the change in Poisson equation $\mu(\mathbf{k}, z)$ defined by

$$-k^2 \tilde{\Psi}(\mathbf{k}, a) = 4\pi G a^2 \tilde{\rho}_m(\mathbf{k}, a) \mu(\mathbf{k}, a) \quad (9)$$

with the Fourier transformed matter density $\tilde{\rho}_m(\mathbf{k}, a)$ and wave-number $k := |\mathbf{k}|$. Note that for $\mu, \eta \rightarrow 1$, GR is retrieved. We know that GR is an excellent description of gravity for very small scales at the very least (Wojtak et al. 2011), hence we force modified gravity to satisfy GR on these scales by the means of screening. There are a variety of proposed screening mechanisms (see Joyce et al. 2015 for an excellent review thereof). The ones most commonly discussed in literature are Chameleon (Khouri & Weltman 2004a,b) and Vainshtein screening (Vainshtein 1972; Babichev & Deffayet 2013). In Chameleon-like screening, the mass of the scalar field depends on the local matter density, making the effects of modified gravity for high-density environments like Earth short-ranged, hence the name. On the other hand, Vainshtein screening suppresses scalar field effects in the presence of massive sources where the ϕ -kinetic terms becomes large. This happens on scales smaller than a characteristic distance named the Vainshtein radius, which is dependent on the properties of the gravity source. In this work, we employ a phenomenological model described in Reischke et al. (2019); Spurio Mancini et al. (2019), where $\eta(k, a)$ and $\mu(k, a)$ decay exponentially to unity for scales smaller than the screening scale $\lambda_s \sim 1/k_s$. In this work, we refrain from testing the effects of implementing a variety of screening mechanisms. However, preliminary results suggest that the approach taken here does not influence the power spectrum up to a few per cent (Grasso et al., in prep.).

One would expect the screening scale to affect extremely non-linear scales and/or high power spectrum amplitudes with the Chameleon or Vainshtein screening. However, we restrict the screening scale to be below intermediate scales, $k_s < 2 \text{ Mpc}^{-1}$ with a fiducial value at $k_s = 0.1 \text{ Mpc}^{-1}$. The reason for only considering (semi-)linear scales is of practical nature: We use HMcode to model the non-linear power spectrum (see also Section 3.3). Notably, HMcode was developed and calibrated for a Λ CDM cosmology and has no inherent knowledge and functionality of modified gravity. While there are efforts to model the non-linear matter power spectrum in scalar-tensor perturbation theory (Cataneo et al. 2019; Bose et al. 2023), there is little similar quan-

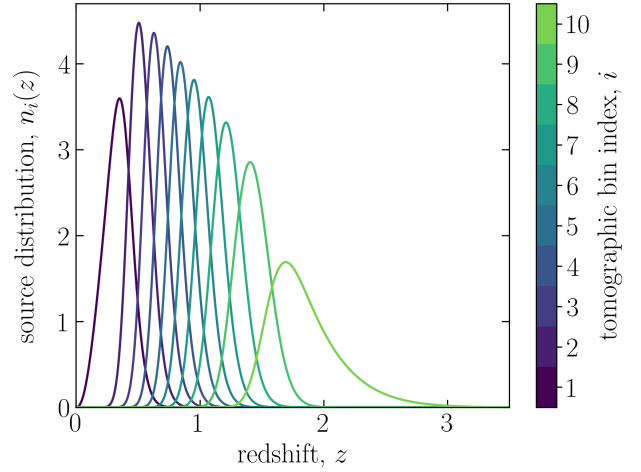


Figure 2. Tomographic source redshift distribution for a stage-4 cosmic shear survey. Adapted to match the EUCLID-CS forecast (Blanchard et al. 2020).

titative research for the baryon power spectrum. To circumvent this issue we remove modified gravity for large k , avoiding the necessity of modelling the effect of modified gravity on baryons. Therefore, including modified gravity on non-linear scales would only increase information gain therein, leaving the results of this work valid as a lower bound.

2.2. Angular power spectrum

We assume the spherical harmonic coefficients $\hat{a}_{\ell m}$ of the fields of interest in this work to follow a zero-mean Gaussian distribution. The measured coefficient consists of a signal ($a_{\ell m}$) and a noise term ($n_{\ell m}^{(a)}$) such that

$$\hat{a}_{\ell m} = a_{\ell m} + n_{\ell m}^{(a)}. \quad (10)$$

Consequently, the angular power spectrum of two fields with coefficients $\hat{a}_{\ell m}, \hat{b}_{\ell m}$ can be split into signal and noise as well:

$$\hat{C}_{\ell}^{AB} = C_{\ell}^{AB} + N_{\ell}^{AB} \delta_{AB}^K, \quad (11)$$

where we defined the angular power spectrum as the non-geometrical component of the correlator such that:

$$\hat{C}_{\ell}^{AB} \delta_{\ell\ell'} \delta_{mm'} = \langle \hat{a}_{\ell m} \hat{b}_{\ell' m'}^* \rangle, \quad (12)$$

for statistically isotropic and homogeneous fields. The Kronecker-Delta, δ_{AB}^K , appears since we assume the noise contributions of the FRB and WL measurement to be uncorrelated. The noise term in Eq. 11 is specific to the type of measurement. However, the signal can be more generally expressed as the projection of the three-dimensional power spectrum $P^{AB}(k, a)$ with the appropriate kernel(s) $W_{A/B}(\chi)$ via the Limber approximation, (Limber 1954) which is sub-percent accurate for $\ell > 10$ (Kilbinger et al. 2017). Including tomographic redshift bins i, j , it can be written as

$$(C_{\ell}^{AB})_{ij} = \int_0^{\chi_H} d\chi \frac{W_A^{(i)}(\chi) W_B^{(j)}(\chi)}{\chi^2} P_{AB} \left(\frac{\ell + \frac{1}{2}}{\chi}, z(\chi) \right) \quad (13)$$

with $\chi_H := \chi(z \rightarrow \infty)$ as the comoving horizon size⁷.

2.2.1. Weak lensing statistics

⁷ Not to be confused with the Hubble distance $\chi_{H_0} = c/H_0$

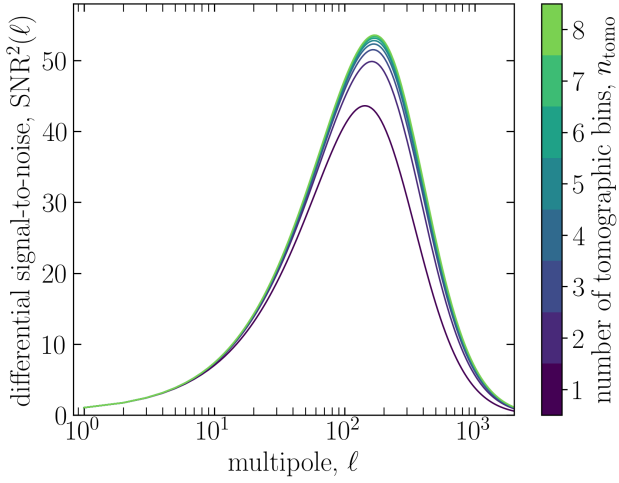


Figure 3. Squared differential SNR dependent on angular scale of the FRB angular power spectrum for different tomographic bin numbers shown as a colour bar.

Shear, commonly denoted with γ , is defined as the trace-free part of the matrix that maps the local light distribution onto the observer image in the presence of a lensing potential ψ . Using a tomographic source distribution $n_{i,\gamma}(z)$, the corresponding kernel (or window function) in GR is given by

$$W_{\gamma,\text{GR}}^{(i)}(\chi) = \frac{3H_0^2}{2c^2} \Omega_{m0} \frac{\chi}{a(\chi)} \int_{\chi}^{\chi_H} d\chi' \frac{\chi' - \chi}{\chi'} n_{i,\gamma}(\chi'), \quad (14)$$

where H_0 is the Hubble constant, Ω_{m0} the matter density parameter today and $n_{i,\gamma}(\chi') d\chi' = n_{i,\gamma}(z) dz$ (Kilbinger 2015)⁸. However, gravity that does not conform with GR naturally affects the distortion of light through WL in a different way. We can absorb non-GR terms originating from matter overdensities into the shear window function, such that

$$W_{\gamma,\text{mod}}^{(i)}(k, \chi) = \frac{1}{2} \mu(k, \chi) \left(1 + \frac{1}{\eta(k, \chi)} \right) W_{\gamma,\text{GR}}^{(i)}(\chi). \quad (15)$$

See Spurio Mancini et al. (2019) for a more detailed derivation, but be aware of the different naming conventions of the Bardeen potentials. The quasi-static approximation (QSA) is often used in the perturbative Einstein equations, where time derivatives are neglected, allowing for an explicit relationship between the α_i and $\mu(k, \chi)$ as well as $\eta(k, \chi)$ (Sawicki & Bellini 2015). However, the `hi_class` modification we use (see also Ch. 3.3) does not employ the QSA. Instead, the density and potential are sourced directly from `hi_class` that considers the full statistical properties of the Weyl potential (Spurio Mancini et al. 2018b). Inserting Eq. 15 with $k = \frac{\ell+1}{2}$ into Eq. 13 with the matter power spectrum P_{mm} yields the auto-correlated cosmic shear angular power spectrum matrix in modified gravity.

The noise component of the observed shear spectra, Eq. 11, called shape noise is given as

$$(N^\gamma)_{ij} = \left(\frac{\sigma_{\epsilon,i}/\sqrt{2}}{\sqrt{\bar{n}_{i,\gamma}}} \right)^2 \delta_{ij}^K. \quad (16)$$

$\sigma_{\epsilon,i}$ is the total intrinsic ellipticity dispersion of sources in tomographic bin i . Typical values are around 0.3 (e.g.

⁸ The transformation $n_i(\chi) d\chi = n_i(z) dz$ holds for the DM source distribution as well.

parameter	description	value
$n_{\epsilon,\text{tomo}}$	tomographic source bins	10
n_{tomo}	tomographic DM bins	4
$\sigma_{\epsilon,i}$	ellipticity dispersion	0.3
$\sigma_{\text{host}0}$ [pc cm ⁻³]	DM dispersion	50
$\bar{n}_{\epsilon,i}$ [arcmin ⁻²]	source density	3
$\bar{n}_{\text{FRB},i}$ [arcmin ⁻²]	FRB density	0.086
f^γ	source sky footprint	0.3
$f^\mathcal{D}$	FRB sky footprint	0.7
ℓ_{max}	maximum angular scale	5000

Table 1. Survey specifications for the mock FRB and stage-4 cosmic shear survey used in the forecast presented here.

Laureijs et al. 2011; Blanchard et al. 2020). $\bar{n}_{i,\gamma}$ is the number of sources per square radiant in tomographic bin i . The shape noise from different redshift bins is uncorrelated as they stem from different sources, and, therefore, the noise contribution is assumed to be diagonal, expressed via δ_{ij}^K .

2.2.2. Dispersion measure statistics

An FRB is a broadband pulse that experiences dispersion when travelling through the intergalactic medium. The time delay of frequency ν accumulated by propagating from source at $l = L$ to observer at $l = 0$ can be measured as $\Delta t \propto \nu^2$, where (up to some physical constants) the proportionality constant is the integrated electron column density along the line of sight dl , also known as the dispersion measure

$$\text{DM} = \int_0^L dl n_e(l). \quad (17)$$

The dispersion caused by the LSS is blended in with dispersion accumulated from the Milky Way (MW) and host galaxy halo where the FRB progenitor resides. Hence, the total DM dependent on angular sky position \hat{n} and redshift z can be written as the sum of its components (Mo et al. 2022):

$$\text{DM}_{\text{tot}}(\hat{n}, z) = \text{DM}_{\text{MW}}(\hat{n}) + \text{DM}_{\text{LSS}}(\hat{n}, z) + \text{DM}_{\text{host}}(z). \quad (18)$$

The LSS contribution can be further split into an isotropic and anisotropic part:

$$\text{DM}_{\text{LSS}}(\hat{n}, z) = \langle \text{DM}_{\text{LSS}} \rangle(z) + \mathcal{D}(\hat{n}, z). \quad (19)$$

In this work, we investigate DM fluctuations $\mathcal{D}(\hat{n}, z)$ which enables us to employ a zero-mean Gaussian field assumption. The corresponding auto-correlated angular power spectrum is then retrieved from Eq. 13 with the electron power spectrum P_{ee} and the DM kernel

$$W_{\mathcal{D}}^{(i)}(\chi) = \mathcal{A} F(z(\chi)) (1 + z(\chi)) \int_{\chi}^{\chi_H} d\chi' n_{i,\mathcal{D}}(\chi') \quad (20)$$

with

$$\mathcal{A} = \frac{3H_0^2 \Omega_{b0}}{8\pi G m_p}, \quad (21)$$

that contains the dimensionless baryon density parameter today Ω_{b0} , the gravitational constant G , the proton mass m_p and the tomographic FRB source distribution $n_{i,\mathcal{D}}(\chi)$. For the fraction of free electrons in the intergalactic medium, $F(z)$, one needs to take into account the fraction of ionised electrons of hydrogen $X_{e,H}(z)$ and helium $X_{e,He}(z)$ with their respective primordial mass fractions Y_H, Y_{He} . Using the total fraction of baryons in the intergalactic medium $f_{\text{IGM}}(z)$, this can

	Parameter	description	fiducial value	prior range	source
investigated parameters	$\hat{\alpha}_B$	braiding function proportionality	0.05	[0, 2.5]	Spurio Mancini et al. (2018b)
	$\hat{\alpha}_M$	Planck mass run rate proportionality	0.05	[0, 3]	Spurio Mancini et al. (2018b)
	$\log_{10}(\frac{k_s}{\text{Mpc}^{-1}})$	Horndeski theory screening scale	-1	[-2, 0.3]	Spurio Mancini et al. (2018b)
	h	dimensionless Hubble parameter	0.674	[0.38, 1.00]	Planck Collaboration et al. (2020b)
	Ω_b	baryon density parameter	0.04931	[0.015, 0.1]	Planck Collaboration et al. (2020b)
	Ω_{cdm}	cold dark matter density parameter	0.2642	[0.18, 0.34]	Planck Collaboration et al. (2020b)
	n_s	primordial scalar index	0.965	[0.7, 1.25]	Planck Collaboration et al. (2020b)
	$\sum m_\nu/\text{eV}$	total mass of all neutrino species	0.06	[0.003, 1.5]	Planck Collaboration et al. (2020b)
	σ_8	linear power spectrum RMS fluctuations	0.811	[0.7, 0.92]	Planck Collaboration et al. (2020b)
	$\log_{10}(\frac{T_{\text{AGN}}}{\text{K}})$	baryonic feedback strength	7.8	[7.0, 8.6]	Mead et al. (2020)
fixed values	N_ν	number of neutrino species	3		Planck Collaboration et al. (2020b)
	M_{Pl}	initial Planck mass	$M_{\text{Pl}}^{\text{obs}}$		-
	$\hat{\alpha}_K$	kineticity function proportionality	1		-
	$\hat{\alpha}_T$	tensor excess speed function proportionality	0		Abbott et al. (2017)
	N_{eff}	effective relativistic degrees of freedom	3.046		Planck Collaboration et al. (2020b)
	T_0	Black body CMB temperature today	2.7255 K		Fixsen (2009)
	z_{reio}	reionisation redshift	7.7		Planck Collaboration et al. (2020b)
	Y_{He}	primordial helium fraction	0.246		Planck Collaboration et al. (2020b)
	$w(a)$	dark energy equation of state	-1		Planck Collaboration et al. (2020b)
	Ω_K	curvature density parameter	0		Planck Collaboration et al. (2020b)

Table 2. Table with the adapted fiducial cosmology and the prior ranges for the different parameters used in this analysis.

be written as

$$F(z) = f_{\text{IGM}}(z) \left[Y_{\text{H}} X_{\text{e,H}}(z) + \frac{1}{2} Y_{\text{He}} X_{\text{e,He}}(z) \right]. \quad (22)$$

However, for the considered redshift range in this work ($z \leq 4$), the intergalactic medium can be assumed to be fully ionised (Aghanim 2001). Additionally, the majority of the DM signal comes from $0.5 < z < 2$ (see also the FRB mock source distribution in Section 3.2.1) at which we assume a constant $f_{\text{IGM}} \approx 0.9$. The exact distribution of baryons is still an object of research (Shull et al. 2012) and a more complex model can be implemented in future work. Combining this assumption with the vanishing fraction of heavy elements ($Y_{\text{H}} \approx 1 - Y_{\text{He}}$), Eq. 22 reduces to

$$F(z) \approx F_{\text{e}} = 0.9 \left[1 - \frac{1}{2} Y_{\text{He}} \right]. \quad (23)$$

A proper model of the MW and host galaxy impact in terms of noise is equally important. Extensive work has been done on the contribution of the MW (Cordes & Lazio 2002; Yao et al. 2017; Yamasaki & Totani 2020) and we assume here that it can be accurately modelled and subtracted. In reality this might not be the case and improper DM_{MW} modelling will lead to large-scale contributions of the DM-DM auto-correlation. However, since shear and DM_{MW} are uncorrelated, we expect the gain in constraining power that is driven by the cross-correlation largely unaffected. Furthermore, selecting FRBs outside of the MW disk would reduce the possible residual non-LSS DM contributions. Meanwhile, the host contribution acts as a Poisson-like flat noise contribution that can be characterised by the host DM dispersion

$$\sigma_{\text{host}}(z) = \frac{\sigma_{\text{host0}}}{1+z} \approx \frac{50 \text{ pc cm}^{-3}}{1+z}. \quad (24)$$

The factor $1+z$ originates from the transformation between the FRB rest- and observer frame (Zhang et al. 2020). The host dispersion is still a large source of uncertainty (Tang et al. 2023). Simulations suggest that the σ_{host0} is rather on order of $\sim 100 \text{ pc cm}^{-3}$ (Kovacs

et al. 2024; Zhang et al. 2024). Still, here we fix the contribution to the observationally motivated value from Arcus et al. (2021). Even though the assumed host dispersion measure might be optimistic, it is highly degenerate with the total number of FRBs (Reischke et al. 2023, Fig. 4 therein). Recent estimates by Connor & Ravi (2023) suggest that the supposed figure of 10000 FRBs until the end of the decade might be on the low end. Thus, we do not expect our choice of parameters to affect the conclusion of this paper. A more rigorous approach would be to additionally marginalise over the host DM dispersion with an analytical model, like we propose in Reischke et al. (2024). However, this is outside the scope of this paper, hence we choose a simplistic host dispersion model. As such, we can write down the noise contribution as

$$(N^{\text{DM}})_{ij} = \left(\frac{\sigma_{\text{host}}(\bar{z}_i)}{\sqrt{n_{i,\text{FRB}}}} \right)^2 \delta_{ij}, \quad (25)$$

where $n_{i,\text{FRB}}$ is the effective number of FRBs per solid angle and

$$\bar{z}_i = \frac{\int_{z_i}^{z_{i+1}} dz n_i(z) z}{\int_{z_i}^{z_{i+1}} dz n_i(z)}. \quad (26)$$

is the weighted mean redshift in bin i . With the formalisms above, the cross-correlated angular power spectrum can be easily obtained by inserting the matter-electron power spectrum

$$P_{\text{em}}(k, z) = \sqrt{P_{\text{ee}}(k, z) P_{\text{mm}}(k, z)} \quad (27)$$

in addition to WL (Eq. 15) and DM (Eq. 20) kernel into Eq. 13.

3. METHODOLOGY

3.1. MCMC likelihood

We forecast the uncertainties on the fiducial set of cosmological parameters $\{\hat{\theta}\}_i$ with a Markov-Chain-Monte-Carlo (MCMC) algorithm. We denote the fiducial spherical harmonic vector as $\hat{\mathbf{a}}_{\ell m}$, with the corresponding power spectrum as $\hat{\mathbf{C}}_{\ell}$. Assuming a Gaussian

likelihood L with covariance $\hat{\mathbf{C}}_\ell$, we can express the expected log-likelihood of measuring $\mathbf{a}_{\ell m}$, given that $\hat{\mathbf{a}}_{\ell m}$ are the true harmonics, as

$$\langle \mathcal{L} \rangle = \langle -\ln(L(\mathbf{a}_{\ell m} | \boldsymbol{\mu} = 0, \hat{\mathbf{C}}_\ell)) \rangle \quad (28)$$

$$= f_{\text{sky}} \sum_{\ell} \frac{2\ell + 1}{2} \text{Tr} \left(\ln(\hat{\mathbf{C}}_\ell) + \hat{\mathbf{C}}_\ell^{-1} \mathbf{C}_\ell \right), \quad (29)$$

where Tr is the trace-operator, $\hat{\mathbf{C}}_\ell^{-1}$ is the inverse of the covariance and the factor $(2\ell + 1)$ originates from the independence of the m -modes which take all integers in the interval $m \in [-\ell, \ell]$ (Tegmark et al. 1997). f_{sky} is a multiplicative factor that effectively decreases the amount of measured m -modes due to partial sky coverage of the used survey (Leistedt et al. 2013; Alonso et al. 2019; Nicola et al. 2021). For a realistic cross-correlation measurement, one has to take into account the effects of differing sky fractions. As an applicable example, consider a measurement of cosmic shear γ and DM fluctuations \mathcal{D} with sky fraction f^γ , $f^\mathcal{D}$ respectively, whereas f^γ is smaller and fully contained in $f^\mathcal{D}$. Furthermore, the full-sky cross-correlation likelihood is calculated with the auto- and cross-correlated angular power spectra matrices

$$\mathbf{C}_\ell = \begin{pmatrix} \mathbf{C}_\ell^{\mathcal{D}\mathcal{D}} & \mathbf{C}_\ell^{\mathcal{D}\gamma} \\ \mathbf{C}_\ell^{\gamma\mathcal{D}} & \mathbf{C}_\ell^{\gamma\gamma} \end{pmatrix} \quad (30)$$

that contain the tomographic angular power spectra defined above. Similarly to our previous analysis (Reischke et al. 2023), the cross-correlated likelihood must be calculated on the smaller footprint f^γ and the contribution from the remaining sky fraction ($f^\mathcal{D} - f^\gamma$) is manually added:

$$\langle \mathcal{L} \rangle^{\mathcal{D}\gamma} = f^\gamma \langle \mathcal{L} \rangle_{\text{full sky}}^{\mathcal{D}\gamma} + (f^\mathcal{D} - f^\gamma) \langle \mathcal{L} \rangle_{\text{full sky}}^{\mathcal{D}}. \quad (31)$$

Note that $\langle \mathcal{L} \rangle_{\text{full sky}}$ is calculated from Eq. 28 with $f_{\text{sky}} = 1$.

3.2. Mock catalogue specification

In the following, we describe the FRB and WL galaxy source distributions adapted for this work.

3.2.1. FRB catalogue

We model the FRB catalogue properties according to a survey that is feasible within the next decade based on the predictions from Petroff et al. (2019). The actual number of host identified FRBs is rapidly growing. They are collected in the comprehensive Blinkverse-database⁹ (Xu et al. 2023). As of the May 2025, there are 92 host identified FRBs. For this analysis, we choose 10^4 FRB samples with associated redshift, whereas a substantial fraction is located above redshift 2. Assuming the FRBs trace the galaxy distribution (Reischke et al. 2021), the source distribution can be written as (assuming a flux limited sample)

$$n(z) \propto z^2 \exp(-\alpha z), \quad (32)$$

where α denotes the survey depth. Henceforth, we use $\alpha = 2.5$ which fulfils the demands above. Note that the current sample of the CHIME survey roughly follows this shape with $\alpha = 4$. However, several surveys are expected to be begin observations in the next years, amongst others the Canadian Hydrogen Observatory and Radio-transient Detector (CHORD, Vanderlinde

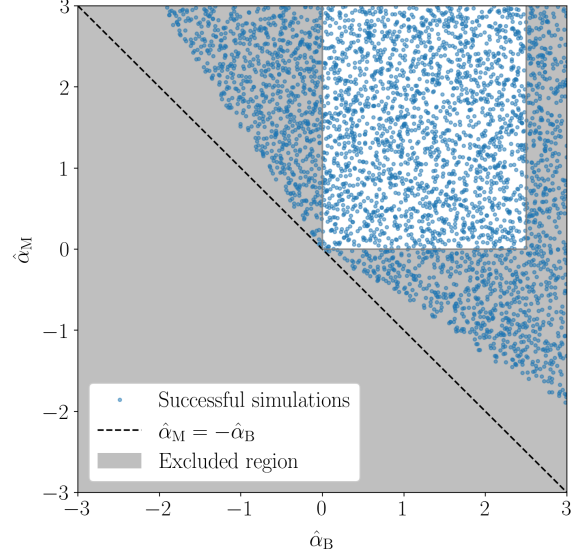


Figure 4. Projection of successful initialisations of `hi_class` from the 11-dimensional hyperspace onto the $\hat{\alpha}_M$ - $\hat{\alpha}_B$ -plane. The blue dots depict the 3881 parameter sets out of 10000 candidates spaced in a Latin Hypercube that did not result in a stability condition break.

et al. 2019) and the Deep Synoptic Array 2000 (DSA-2000, Hallinan et al. 2019). The latter one is expected to commence survey in March 2026 with an annual localised FRB detection rate of 10^4 and within 3.5 arcsec resolution, yielding a substantially larger detection rate and increased survey depth in comparison to CHIME, see Connor & Ravi (2023) for a more comprehensive review. We thus expect $\alpha = 2.5$ to be more representative of the actual redshift distribution feasible within the next years. We split the redshift distribution into four equipopulated redshift bins (see also Tanidis & Camera 2019), thus recovering depths information and increasing the signal-to-noise ratio (SNR). We estimate the SNR from the Fisher information matrix (Tegmark et al. 1997) by treating the signal amplitude A defined by $\hat{\mathbf{C}}_\ell = A\hat{\mathbf{S}}_\ell + \hat{\mathbf{N}}_\ell$ as a cosmological parameter, in which case the cumulative SNR can be calculated as

$$\begin{aligned} \Sigma^2(\leq \ell_{\text{max}}) &= \sum_{\ell=1}^{\ell_{\text{max}}} \text{SNR}^2(\ell) \\ &= f_{\text{sky}} \sum_{\ell=1}^{\ell_{\text{max}}} \frac{2\ell + 1}{2} \text{Tr} \left(\hat{\mathbf{C}}_\ell^{-1} \hat{\mathbf{S}}_\ell \hat{\mathbf{C}}_\ell^{-1} \hat{\mathbf{S}}_\ell \right), \end{aligned} \quad (33)$$

where $\hat{\mathbf{S}}_\ell$, $\hat{\mathbf{C}}_\ell$ are the fiducial angular power spectrum matrices without noise and with noise, respectively, and ℓ_{max} denotes the maximal measured multipole. In Fig. 3 the differential SNR for different numbers of tomographic redshift bins is depicted. For $n_{\text{tomo}} > 4$ the gain saturates, hence we will use this as our baseline. One can also see that the SNR peaks around $\ell \sim 200$ due to the relatively large noise contribution which starts dominating at this angular scale.

With the sky coverage factor $f^\mathcal{D}$, the total amount of measured FRBs n_{FRB} and the number of tomographic redshift bins n_{tomo} , the effective number of FRBs per solid angle ($\bar{n}_{\text{FRB},i}$) in radians becomes

$$\bar{n}_{\text{FRB},i} = \frac{n_{\text{FRB}}}{4\pi f^\mathcal{D} n_{\text{tomo}}}. \quad (34)$$

⁹ <https://blinkverse.zero2x.org/>

Parameter	FRB	Euclid-CS	Euclid-CS×FRB	reduction factor for $\hat{\alpha}_{B/M}^{\text{fid}} = 0.05$ ($\hat{\alpha}_{B/M}^{\text{fid}} = 1$)
Ω_b	$0.044^{+0.006}_{-0.010}$	$0.049^{+0.011}_{-0.010}$	$0.0482^{+0.0029}_{-0.0025}$	3.8 (3.8)
Ω_{cdm}	0.240 ± 0.023	0.259 ± 0.012	0.2637 ± 0.0031	3.9 (3.3)
h	0.78 ± 0.11	$0.819^{+0.140}_{-0.094}$	$0.690^{+0.030}_{-0.044}$	3.1 (2.9)
n_s	0.98 ± 0.13	$0.904^{+0.089}_{-0.070}$	$0.954^{+0.034}_{-0.028}$	2.5 (2.0)
$\sum m_\nu/\text{eV}$	< 0.758	< 0.455	< 0.104	4.5 (3.1)
$\log_{10}\left(\frac{T_{\text{AGN}}}{\text{K}}\right)$	$7.817^{+0.069}_{-0.059}$	$7.76^{+0.24}_{-0.19}$	$7.7990^{+0.0087}_{-0.0078}$	25.9 (16.8)
σ_8	$0.798^{+0.032}_{-0.096}$	$0.8097^{+0.0040}_{-0.0056}$	0.8116 ± 0.0040	1.3 (1.4)
$\hat{\alpha}_B$	< 1.53	$0.83^{+0.31}_{-0.72}$	< 0.618	1.6 (1.7)
$\hat{\alpha}_M$	—	< 1.64	< 1.20	1.4 (1.5)
$\log_{10}\left(\frac{k_s}{\text{Mpc}^{-1}}\right)$	—	< -1.46	< -1.46	1.0 (1.6)

Table 3. Posterior mean with 68% confidence intervals for the auto- and cross-correlations of DM and shear fluctuations with the fiducial values presented in Tab. 2. The reduction factor relates to the improvement from Euclid-CS×FRB as opposed to Euclid-CS alone and is shown for the case $\hat{\alpha}_{B/M}^{\text{fid}} = 0.05$ and $\hat{\alpha}_{B/M}^{\text{fid}} = 1$ in brackets in the last column.

The specifications for the FRB redshift bins are shown in Tab. 1 and the source distribution is depicted in Fig. 1.

Discontinuities between the FRB bins originate from the individual normalisation of the source distribution in each bin, such that all $n_i(z)$ are proper probability distribution. Note that we use a simplistic mock FRB catalogue, which implicitly assumes full knowledge of the DM- z relation. In reality, the real redshift of the FRB progenitor is often unknown. That can lead to a multitude of unaccounted for effects in this pipeline, such as the scattering of sources between different redshift bins, similarly to the photometric redshift scatter known from shear analyses (Dahlen et al. 2013, Euclid Collaboration et al. 2020b). While this mock catalogue is a suitable starting point to estimate the performance of future FRB surveys, we refer the reader to future analyses for more elaborate FRB catalogues.

3.2.2. Shear catalogue

We adapt a stage-4 WL survey with properties given in Euclid Collaboration et al. (2020a). The corresponding specifications can be found in Tab. 1 and the source-redshift distribution is shown in Fig. 2. We will henceforth refer to the WL survey as Euclid-Cosmic-Shear (Euclid-CS) in the remainder of the paper.

3.3. Three dimensional power spectrum generation

We calculate the linear matter power spectrum with the Boltzmann solver **Horndeski** in **class** (**hi_class**¹⁰, Zumalacárregui et al. 2017, Bellini et al. 2020) suite which is an extension to the **Cosmic Linear Anisotropy Solving System** code (**class**¹¹, Blas et al. 2011). Subsequently, utilising **pycc1**¹² (Chisari et al. 2019b), we pass the linear matter power spectrum into **HMcode**¹³ (Mead et al. 2015) to calculate the non-linear matter and electron power spectrum P_{mm} , P_{ee} and, consequently, the electron bias via

$$b_e^2(k, z) = \frac{P_{\text{ee}}(k, z)}{P_{\text{mm}}(k, z)}, \quad (35)$$

where we employ the halo model designated as **HMx2020_matter_pressure_w_temp_scaling** (Mead et al. 2020). The full list of cosmological parameters with their respective fiducial values is shown in Tab. 2.

Generating thousands of samples from **hi_class** for the MCMC is computationally expensive, in particular if we want to run multiple analyses with varying hyperparameters. Thus, we employ **cosmopower**¹⁴ (Spurio Mancini et al. 2022) to train and emulate the nonlinear matter power spectrum P_{mm} , the electron bias b_e , the comoving distance χ and the modified gravity functions μ, η . The latter two are calculated using a modified **hi_class** code from Spurio Mancini et al. (2018b). By initialising **hi_class** with the parameters and prior bounds from Tab. 2, we simulated 190173 training and 9793 testing sets in a Latin-Hyper-Cube, meaning they are semi-randomly evenly distributed across the whole hyperspace. Note that we are limited to a one-dimensional output layer due to the nature of neural networks, hence we treat the redshift dependency of the individual functions as a cosmological parameter with bounds $z \in [0, 4.5]$ the emulator needs to be trained on. In total, we map the (10+1)-parameter input space to a 200 parameter space consisting of k -values logarithmically spaced in $k \in [10^{-5}, 150] \text{ Mpc}^{-1}$. The highly non-linear upper bound is a numerical necessity caused by the limber approximation since

$$k_{\text{max}} = \frac{\ell_{\text{max}} + 1/2}{\chi(z_{\text{min}} = 10^{-2})} \approx 113 \text{ Mpc}^{-1}$$

in Planck cosmology. The majority of signal resides around $\ell \sim \mathcal{O}(200)$ (see also Fig. 3) for FRBs. While cosmic shear obtains a significant signal from larger ℓ , contributions for $k > 50 \text{ Mpc}^{-1}$ will generally be small. For more details on the emulator choices we refer to appendix B.

Finally, with the emulators we can calculate the angular power spectra detailed in Section 2, which in turn enables us to obtain the log-likelihood (Eq. 28) for any cosmology contained in the prior ranges from Tab. 2. Hence, by sampling the likelihood with the Importance Nested Sampling Algorithm (INS, Feroz et al. 2019) using **Nautilus-sampler**¹⁵ (Lange 2023), we obtain the posterior probability density.

4. RESULTS

We show the 68% and 95% confidence regions for the three cases, i.e. WL and FRBs alone as well as WL × FRBs in Fig. 5. Overall, FRBs have considerably less constraining power than WL alone

¹⁰ http://miguelzuma.github.io/hi_class_public/

¹¹ https://github.com/lesgourg/class_public

¹² <https://github.com/LSSTDESC/CCL>

¹³ <https://github.com/alexander-mead/HMcode>

¹⁴ <https://github.com/alessiospurioimancini/cosmopower>

¹⁵ <https://github.com/johannesulf/nautilus.git>

Assuming weak modified gravity with $\hat{\alpha}_B^{\text{fid}} = \hat{\alpha}_M^{\text{fid}} = 0.05$

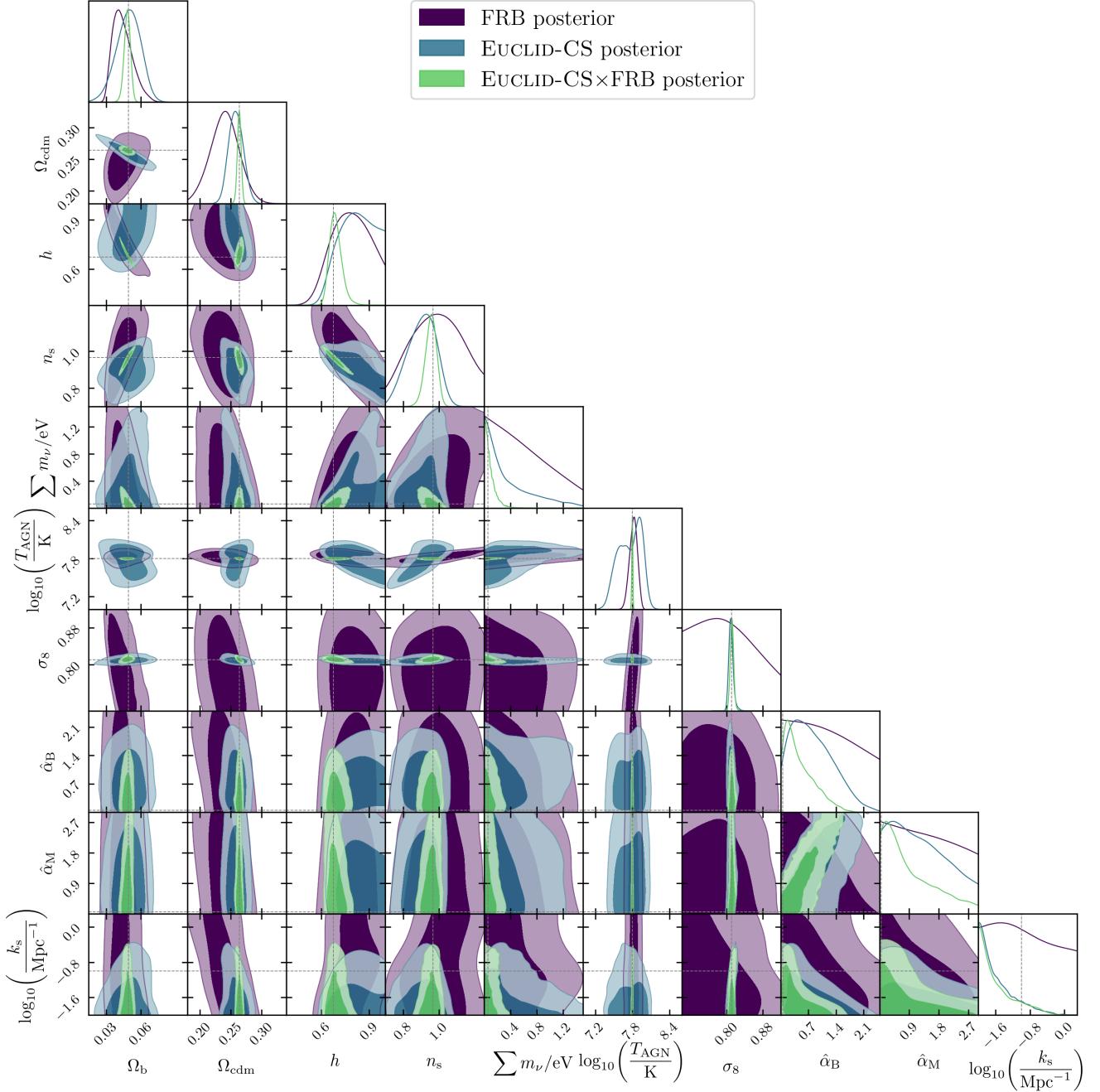


Figure 5. 68% and 95 % posterior confidence regions (dark and light areas, respectively) for FRB and EUCLID-CS auto-correlation and their cross-correlation. The fiducial cosmology taken from Tab. 2 is indicated by grey, dashed lines.

due to the overall lesser SNR, as WL from a stage-4 survey have a cumulative SNR which is roughly 10 times higher than the one of the FRB mock survey assumed here. Consequently, also the constraints on modified gravity are generally weaker. However, FRBs impose much smaller uncertainties on the baryon density $\Omega_b h^2$ and the baryonic feedback strength $\log_{10}(\frac{T_{\text{AGN}}}{\text{K}})$. The latter has been extensively discussed in our previous analysis (Reischke et al. 2023), hence we will refrain from detailing this effect here. Nevertheless, it should be noted that we expect a majority of the cross-correlation improvement to originate from degeneracy breaking due to baryonic feedback calibration with FRBs. Indeed, when cross-correlating shear and DM, the confidence regions of almost all parameters shrink significantly. The marginalised posterior mean and the 68% confidence intervals are quantified in Tab. 3. After $\log_{10}(\frac{T_{\text{AGN}}}{\text{K}})$, the

parameters describing the energy contents of the Universe ($\sum m_\nu$, Ω_b , Ω_c) experience the greatest increase in precision. Looking at the Ω_b - h degeneracy apparent in Fig. 5, a separate calibration of h further tightens the obtained constraints. In appendix A, we show the posterior for combining EUCLID-CS x FRB with the PLANCK2018 (Planck Collaboration et al. 2020a) temperature anisotropy auto-correlation. This breaks the degeneracy Ω_b - h , leading to much tighter constraints. Walters et al. (2018) similarly forecasted competitive constraining power when combining FRBs with distance ladder measurement on the background level. Since FRBs can be considered a late-type cosmological probe, this is a sensible addition for future analyses. A smaller but still considerable amount of gain is seen for the primordial power spectrum scale dependency n_s , possibly caused by the comparatively large signal of FRBs for

Assuming strong modified gravity with $\hat{\alpha}_B^{\text{fid}} = \hat{\alpha}_M^{\text{fid}} = 1$

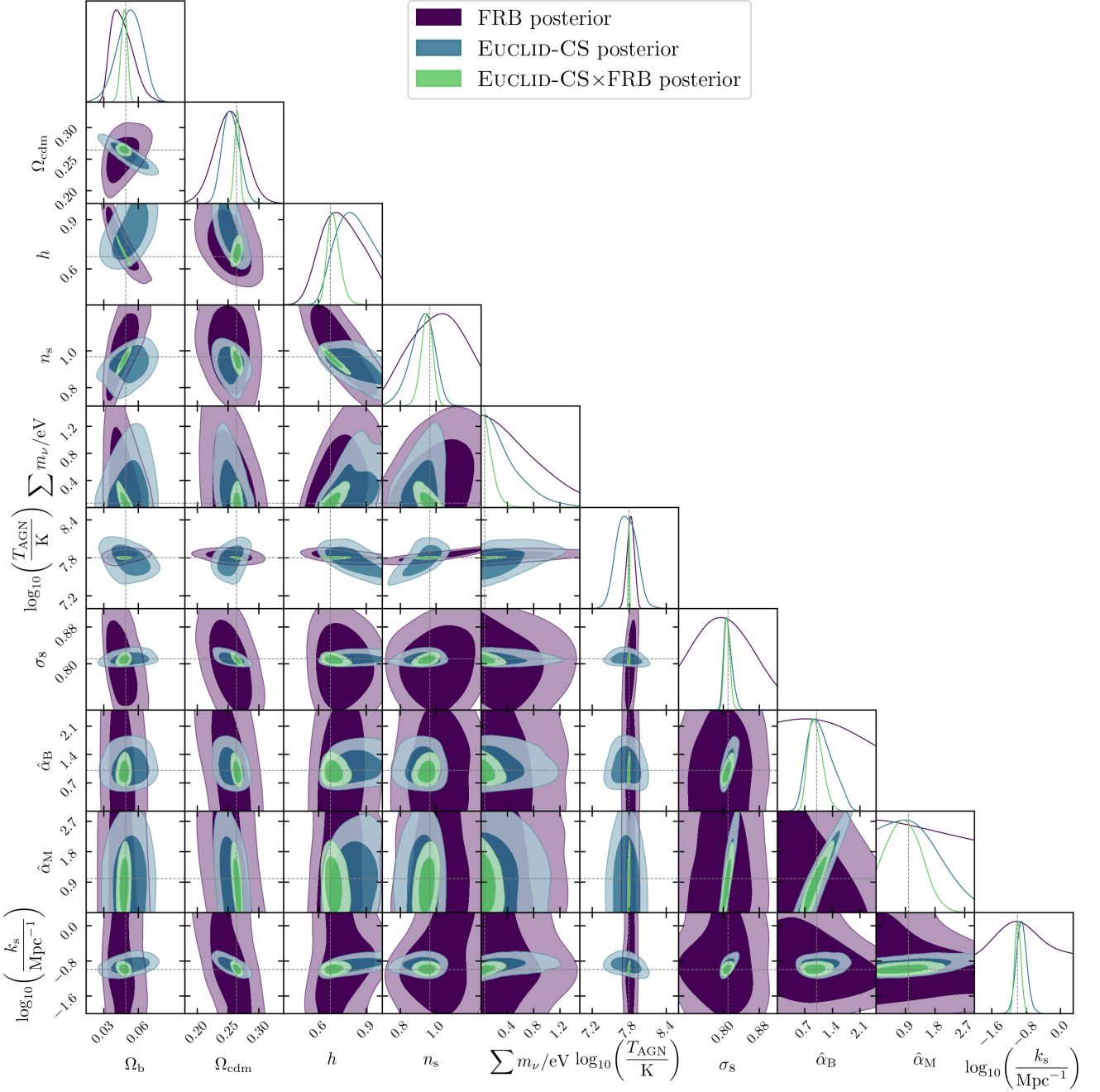


Figure 6. 68% and 95 % posterior confidence regions (dark and light areas, respectively) for FRB and EUCLID-CS auto-correlation and their cross-correlation. The fiducial cosmology from Tab. 2 is used except for $\hat{\alpha}_M = \hat{\alpha}_B = 1$.

small k , at which n_s still determines the slope.

On the contrary, little information can be drawn for σ_8 in contrast to the WL measurement, leading to only a $\sim 20\%$ improvement for the cross-correlation. The improvement of $\hat{\alpha}_{M/B}$ is on a similar order of magnitude, putting them amongst the most weakly constrained parameters. Nevertheless, a $\sim 30 - 40\%$ reduction is detectable, likely originating from degeneracy breaking between other cosmological parameters and general accessibility of more large scale modes. However, most notably, the $\log_{10}(\frac{k_s}{\text{Mpc}^{-1}})$ posterior has a peculiar behaviour. Including FRBs into the analysis has almost no discernible effect on the precision of this measurement. Additionally, we forecast a bias of the posterior towards low screening scales k_s . WL in particular tends to underpredict this parameter. This is due to projection effects of the full posterior when showing marginalised con-

tours. As the modified gravity parameters are bounded from below by Λ CDM there is a bunching up of probability in this region when the fiducial (i.e. the real Universe) is very close to Λ CDM. Since $\log_{10}(\frac{k_s}{\text{Mpc}^{-1}})$ has no effect in Λ CDM, the posterior is just the prior in this case. Therefore, the projection to a marginalised contour can appear to bias the parameters. Increasing the prior range to lower bounds would thus not increase the gain in information, apart from removing almost any modified gravity effects altogether.

Further peculiar behaviour can be seen for the $\log_{10}(\frac{T_{\text{AGN}}}{\text{K}})$ -EUCLID-CS posterior in Fig. 5; displaying a bimodal distribution. While a Gaussian probability distribution cannot be expected in an MCMC, specifically the modified gravity parameter contour shapes show large deviations thereof caused by limiting prior

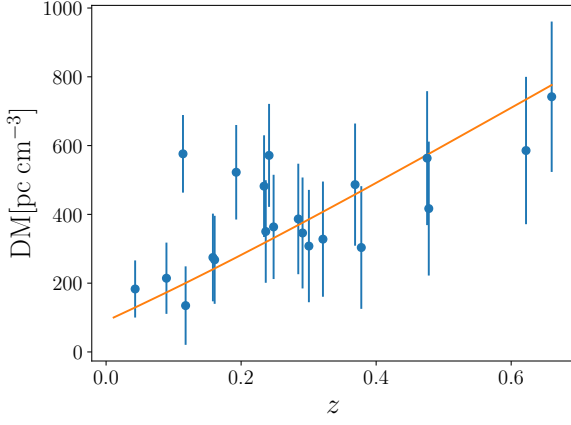


Figure 7. FRB with host identification used in this study. The error bars are a sum of $\sigma_{\text{MW}} = 50$, $\sigma_{\text{host}} = 50/(1+z)$ and the cosmological contribution from Eq. 36. The orange line corresponds to the best-fit model.

ranges. We excluded significant influence from the MCMC-algorithm as the underlying cause (see App. C). Considering the strong deviation of the predicted k_s to the fiducial one, we conclude that the contours from Fig. 5 to be strongly influenced by the informative prior we place on $\hat{\alpha}_{\text{B/M}}$ and k_s .

The motivation behind this choice is of both physical and numerical nature. In principle, $\hat{\alpha}_{\text{B/M}}$ can be negative (Bellini & Sawicki 2014) and even are expected to in many of the commonly investigated scalar-field theories like $f(R)$ (Carroll et al. 2004) or Galileon cosmology (Chow & Khoury 2009). However, $\hat{\alpha}_{\text{B/M}} < 0$ can lead to gradient instabilities produced by an imaginary sound speed that causes exponentially growing perturbations (Zumalacárregui et al. 2017). Even on the theoretically stable $\hat{\alpha}_{\text{M}} = -\hat{\alpha}_{\text{B}}$ line, numerical fluctuations can lead to the aforementioned runaway effect. We demonstrate this effect by showing the $\hat{\alpha}_{\text{M}} - \hat{\alpha}_{\text{B}}$ parameter-space with successfully initialised `hi_class` instances in Fig. 4. Note that we simulate within the prior ranges from Tab. 2 except for the braiding and Planck mass run rate, which we extend to $\hat{\alpha}_{\text{B/M}} \in [-3, 3]$. Thus, while certain sets of negative parameters are stable (Spurio Mancini et al. 2019), uniform and independent priors for $\hat{\alpha}_{\text{B}}$ and $\hat{\alpha}_{\text{M}}$ are only possible for positive values thereof, hence the choice in this work. Additionally, we exclude $\hat{\alpha}_{\text{B}} > 2.5$ due to a decreased density of successful `hi_class` initialisations there as well.

To circumvent the issues of those projection affects, we additionally run our analysis for a “strong fiducial modified gravity” ($\hat{\alpha}_{\text{B/M}}^{\text{fid}} = 1$) as opposed to the previously used “weak fiducial modified gravity” ($\hat{\alpha}_{\text{B/M}}^{\text{fid}} = 0.05$). We know from the PLANCK CMB survey (Planck Collaboration et al. 2016) that we live at least in a close-to- Λ CDM Universe. Still, by increasing the fiducial braiding and Planck mass run rate parameters, we move them away from the prior edges and, hence, mimic looser boundaries. We do not quote the marginalised posterior uncertainties explicitly, but show the improvement when using FRBs in brackets in the last column of Tab. 3. However, we show the contours in Fig. 6. First, one should notice that much of the peculiar behaviour of the WL contours vanish in strong modified gravity; the WL $\log_{10}(\frac{T_{\text{AGN}}}{\text{K}})$ posterior is no longer bimodal and the measurements of k_s are not biased towards lower values anymore. The screening scale recovered now is on par with the fiducial input screening scale, chosen such as to suppress modified gravity in

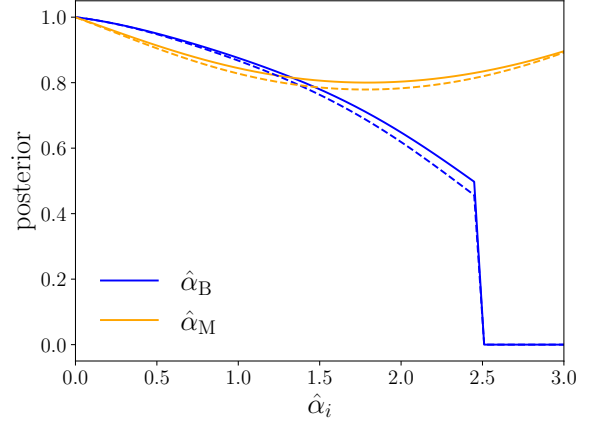


Figure 8. Posterior distribution of $\hat{\alpha}_{\text{B}}$ (blue) and $\hat{\alpha}_{\text{M}}$ (orange) assuming a Gaussian (lognormal) host model in solid (dashed). The cutoff of $\hat{\alpha}_{\text{B}}$ originates from prior limitations due to `hi_class` instabilities (see also Fig. 4).

the non-linear regime (see also Spurio Mancini et al. 2018b).

Consequently, the 68% confidence intervals change slightly as well. Even though FRBs still can not constrain modified gravity alone, the improvement of $\hat{\alpha}_{\text{B}}$ from WL auto-correlation to WL-FRB cross-correlation slightly increases to 42.5% and the one of $\hat{\alpha}_{\text{M}}$ to 31.1%. Many of the other parameter improvements are comparable to the weak modified gravity case, except for n_s and σ_8 which respectively decrease and increase marginally in strong modified gravity. Therefore, we expect to gain constraining power on modified gravity when cross-correlating FRBs with WL, albeit less sizeable than for baryon-related parameters. Adding CMB temperature anisotropy information has little effect on the modified gravity parameter contours, indicating only weak correlation between $\hat{\alpha}_{\text{B/M}}$ and h , Ω_b , n_s (see appendix A).

5. APPLICATION TO FRBS WITH HOST

In this section, we use FRBs with host identification to provide some upper bounds on modified gravity. This is very similar to the methodology outlined in Reischke & Hagstotz (2023b,a) where the sensitivity is in the covariance between the different data points of the measurement of the DM- z relation, i.e. probing correlations between different lines-of-sight. There are already some analyses of statistical properties of the signal via cross-correlation with the LSS (e.g. CHIME/FRB Collaboration et al. 2021) or using targeted galaxy surveys to reduce cosmic variance (Khrykin et al. 2024). However, the quality of the current data is not good enough yet to carry out the analysis proposed in the previous section. The LSS covariance of two FRBs observed at redshift z_i, z_j and with pairwise separation θ_{ij} can be calculated as

$$\text{cov}_{ij}(\cos \theta, z_i, z_j) = \sum_{\ell} \frac{2\ell + 1}{4\pi} P_{\ell}(\cos \theta) (C_{\ell}^{\text{DD}})_{ij}, \quad (36)$$

where we use a δ -distribution for the redshift distribution in Eq. 20 selecting redshift z_i and z_j . Here the Legendre polynomials are denoted as $P_{\ell}(x)$.

Assuming a distribution for the host, p_{host} , the final likelihood is given by:

$$p(\text{DM}|\theta) = \int_0^{\infty} d\text{DM}_{\text{host}} p_{\text{host}}(\text{DM}_{\text{host}}) \times p_{\text{LSS}}(\text{DM} - \text{DM}_{\text{host}}), \quad (37)$$

where $(\mathbf{DM}_{\text{host}})_i = \text{DM}_{\text{host}}/(1+z_i)$ and p_{LSS} is a Gaussian with covariance with components given by Eq. 36 and the components of the mean by:

$$\text{DM}_{\text{LSS}}(z_i) = \int_0^{\chi(z_i)} d\chi' W_{\mathcal{D}}^{(i)}(\chi'). \quad (38)$$

In Fig. 7 we show the FRBs used for this analysis together with the best fit model, see Tab. 5 in the Appendix for a comprehensive list. The error includes the covariance contribution from the LSS, from the host and from the Milky Way. Due to the low number of FRBs, we maximize the likelihood with respect to the ΛCDM parameters and then scan the profiles of $\hat{\alpha}_{\text{M}}$ and $\hat{\alpha}_{\text{B}}$ respectively. This removes the issue of projection effects and allows to get the most stringent constraints from the current data set. Fig. 8 shows this likelihood scan, showing that the posterior is prior driven (see Tab. 2). Note that the sharp cut-off in $\hat{\alpha}_{\text{B}}$ is caused by the introduced emulator boundaries. There seems to be no information regarding $\hat{\alpha}_{\text{M}}$ with the current data. While there is a slight constraint on $\hat{\alpha}_{\text{B}}$, this is not significantly different from the prior. Generally this behaviour is expected as the parameter dependence is only present in the perturbations and thus in the covariance, degrading the information content compared to the model. However, it goes to show that host-identified FRBs are in principle a versatile tool to test gravity, in particular with many more sources expected in the next years (e.g. with DSA-2000, Hallinan et al. 2019)

6. SUMMARY

In this paper, we investigated the prospects to constrain modified gravity with the DM of FRB and WL, as well as their cross-correlation. We calculated the linear Horndeski-type perturbations of GR (i.e. a metric theory with an additional scalar degree of freedom) that acts on the bardeen potentials Φ and Ψ . Non-linear correction to that model has been applied with ΛCDM corrections using **HMcode** with baryonic feedback controlled by a linear interpolation of a one-parametric model. Since FRBs show a substantial signal-to-noise ratio for small k -scales while being very sensitive to baryonic effects, they complement WL. We employed the Boltzmann-solver **hi_class** to simulate the background cosmology and linear perturbations thereof governed by modified gravity. By propagating the results through **HMcode**, we obtain the non-linear corrections to the three-dimensional matter and electron power spectra in a ΛCDM cosmology. We ensure screening by introducing a free parameter k_s so that GR is recovered for $k > k_s$. The three-dimensional power spectra are then projected onto angular space with the specified EUCLID-CS and 10000 sources-FRB survey. This 10-parameter model is sensitive to modified gravity on linear scales, baryonic effects and matter clustering and can be a starting point for future WL×FRB large-scale structure analyses. To speed up calculations, we trained a **cosmopower** neural network to emulate the statistical properties of the Bardeen potentials and the matter and the electron power spectrum. We carried out three types of analysis:

- i) First, we investigated a weak modified gravity case with fiducial linear Planck mass run rate and braiding proportionality constant set to $\hat{\alpha}_{\text{M}}^{\text{fid}} = \hat{\alpha}_{\text{B}}^{\text{fid}} = 0.05$. In this case, the forecast is dominated by the $\hat{\alpha}_{\text{M/B}}$ prior edges that exclude negative values. We additionally detect a

preference for low values of the screening scale k_s . However, the posterior is generally rather unconstrained, which we believe to be a consequence of the fiducial cosmology at which the data was drawn. Nevertheless, by combining 10000 FRBs with redshift information with a EUCLID-CS-like survey, the $\hat{\alpha}_{\text{M}}$ and $\hat{\alpha}_{\text{B}}$ 68%-constraints improve by a factor of 1.4 and 1.6 respectively, in comparison to the constraints from EUCLID-CS alone.

- ii) We repeat the same analysis with strong fiducial modified gravity case with $\hat{\alpha}_{\text{M}}^{\text{fid}} = \hat{\alpha}_{\text{B}}^{\text{fid}} = 1$. Here the posteriors are no longer prior dominated and k_s -bias is no longer detectable. The improvement from WL to WL×FRB changes to a factor of 1.7, 1.5 and 1.6 for $\hat{\alpha}_{\text{M}}$, $\hat{\alpha}_{\text{B}}$ and $\log_{10}(\frac{k_s}{\text{Mpc}^{-1}})$ respectively. FRBs alone put little constraints on Horndeski theory, so the majority of signal in the cross-correlation with WL likely originates from degeneracy breaking between other cosmological parameters. It has already been established that FRBs are highly sensitive to the intergalactic baryonic component, which is where a majority of the signal resides in this work as well. Nevertheless, a 50% decrease in the error bars makes an implementation of FRBs into future modified gravity investigations worthwhile.
- iii) An analysis of 21 FRBs with host identification where the dependence of modified gravity is expressed in the covariance of the DM – z relation of the FRBs. The constraints on modified gravity are prior dominated in this case with a small bit of information added for $\hat{\alpha}_{\text{B}}$, consistent with the other findings.

During the weak modified gravity analysis, core limitations of the underlying modelling became apparent. Even though many scalar-tensor perturbations of GR require a negative scaling of the braiding or Planck mass run rate with dark energy, this parameter space is largely unstable, and thus uncontrollable, in the current **hi_class** release. This is in large part due to the obvious necessity of non-imaginary primordial baryon sound velocity. That being said, because of numerical fluctuations the $\hat{\alpha}_{\text{M}} = -\hat{\alpha}_{\text{B}}$ line is non-accessible as well, despite the fact that is physically conceivable. While we can derive some limits as demonstrated above, the current state of general, numerical Horndeski theory tools is not fit for large-scale cosmological analyses, yet. Possible refinements for **hi_class** could include shifting the parameterisation from $\hat{\alpha}_{\text{M}}$ or $\hat{\alpha}_{\text{B}}$ to the sound velocity c_s^2 such that small numerical deviations can not lead to a runaway gradient. In a recent development, Cataneo & Bellini (2024) built the *Modelling Optimisation to Compute Horndeski in CLASS* (**mochi_class**¹⁶) suite, which might be able to address some of these issues in future analyses.

Generally, we find FRBs to be a versatile assisting tool for WL to constrain the nature of gravity. While they are not very sensitive to modifications to gravity by themselves, they allow to break degeneracies in other parameters and constrain baryonic feedback (Reischke et al. 2023), thus freeing up more WL signal to be used for the measurement of the gravitational slip. FRBs are thus a suitable addition to other LSS probes like WL that will soon likely gain enough precision to confirm or

¹⁶ https://github.com/mcataneo/mochi_class_public

rule out such scalar perturbations, causing the necessity of accurate modified gravity modelling tools.

ACKNOWLEDGEMENTS

During parts of this work, RR was supported by a European Research Council Consolidator Grant (No. 770935). DN acknowledges funding from the European Research Council (ERC) under the European Union's Horizon 2020 research and innovation program (Grant agreement No. 101053992). SH was supported by the Excellence Cluster ORIGINS which is funded by the Deutsche Forschungsgemeinschaft (DFG, German Research Foundation) under Germany's Excellence Strategy - EXC-2094 - 390783311. RR is supported by the ERC (Grant No. 770935). H. Hildebrandt is supported by a DFG Heisenberg grant (Hi 1495/5-1), the DFG Collaborative Research Center SFB1491, an ERC Consolidator Grant (No. 770935), and the DLR project 50QE2305.

REFERENCES

- Abbott B. P., et al., 2017, *ApJ*, 848, L13
- Adi T., Kovetz E. D., 2021, *Phys. Rev. D*, 104, 103515
- Aghanim N., 2001, *New A Rev.*, 45, 303
- Alonso D., Bellini E., Ferreira P. G., Zumalacárregui M., 2017, *Phys. Rev. D*, 95, 063502
- Alonso D., Sanchez J., Slosar A., LSST Dark Energy Science Collaboration 2019, *MNRAS*, 484, 4127
- Arcus W. R., Macquart J. P., Sammons M. W., James C. W., Ekers R. D., 2021, *MNRAS*, 501, 5319
- Auclair P., et al., 2023, *Living Rev. Relativ.*, 26, 5
- Babichev E., Deffayet C., 2013, *Classical Quant. Grav.*, 30, 184001
- Bannister K. W., et al., 2019, *Science*, 365, 565
- Bardeen J. M., 1980, *Phys. Rev. D*, 22, 1882
- Bellini E., Sawicki I., 2014, *J. Cosmology Astropart. Phys.*, 7, 050
- Bellini E., Cuesta A. J., Jimenez R., Verde L., 2016, *J. Cosmology Astropart. Phys.*, 02, 053
- Bellini E., Sawicki I., Zumalacárregui M., 2020, *J. Cosmology Astropart. Phys.*, 2020, 008
- Bhandari S., Kumar P., Shannon R. M., Macquart J. P., 2019, *The Astronomer's Telegram*, 12940, 1
- Bhandari S., et al., 2022, *AJ*, 163, 69
- Bhattacharya M., Kumar P., Linder E. V., 2021, *Phys. Rev. D*, 103, 103526
- Blanchard A., et al., 2020, *Astron. Astrophys.*, 642, A191
- Blas D., Lesgourgues J., Tram T., 2011, *J. Cosmology Astropart. Phys.*, 07, 034
- Bose B., Tsedrik M., Kennedy J., Lombriser L., Pourtsidou A., Taylor A., 2023, *MNRAS*, 519, 4780
- CHIME/FRB Collaboration et al., 2021, *ApJS*, 257, 59
- Carroll S. M., Duvvuri V., Trodden M., Turner M. S., 2004, *Phys. Rev. D*, 70, 043528
- Cataneo M., Bellini E., 2024, *Open J. Astroph.*, 7
- Cataneo M., Lombriser L., Heymans C., Mead A. J., Barreira A., Bose S., Li B., 2019, *MNRAS*, 488, 2121
- Chisari N. E., et al., 2019a, *Open J. Astroph.*, 2
- Chisari N. E., et al., 2019b, *ApJS*, 242, 2
- Chow N., Khoury J., 2009, *Phys. Rev. D*, 80, 024037
- Connor L., Ravi V., 2023, *MNRAS*, 521, 4024
- Cordes J. M., Lazio T. J. W., 2002, NE2001.I. A New Model for the Galactic Distribution of Free Electrons and its Fluctuations, [doi:10.48550/arXiv.astro-ph/0207156](https://arxiv.org/abs/10.48550/arXiv.astro-ph/0207156)
- DESI Collaboration et al., 2025, *J. Cosmology Astropart. Phys.*, 2025, 021
- Dahlen T., et al., 2013, *ApJ*, 775, 93
- De Rham C., Melville S., 2018, *Phys. Rev. Lett.*, 121, 221101
- Dewdney P. E., Hall P. J., Schilizzi R. T., Lazio T. J. L. W., 2009, *Proc. IEEE*, 97, 1482
- Escamilla L. A., Giarè W., Valentino E. D., Nunes R. C., Vagnozzi S., 2024, *J. Cosmology Astropart. Phys.*, 2024, 091
- Euclid Collaboration et al., 2020a, *A&A*, 642, A191
- Euclid Collaboration et al., 2020b, *A&A*, 644, A31
- Ezquiaga J. M., Zumalacárregui M., 2017, *Phys. Rev. Lett.*, 119, 251304
- Feroz F., Hobson M. P., Cameron E., Pettitt A. N., 2019, *Open J. Astroph.*, 2
- Fixsen D. J., 2009, *ApJ*, 707, 916
- Hagstotz S., Reischke R., Lilow R., 2022, *MNRAS*, 511, 662
- Hallinan G., et al., 2019, The DSA-2000 — A Radio Survey Camera, [doi:10.48550/arXiv.1907.07648](https://arxiv.org/abs/10.48550/arXiv.1907.07648)
- Hashimoto T., et al., 2020, *MNRAS*, 497, 4107
- Heisenberg L., 2019, *Phys. Rep.*, 796, 1
- Horndeski G. W., 1974, *Int. J. Theor. Phys.*, 10, 363
- James C. W., et al., 2022, *MNRAS*, 516, 4862
- Jiang X., Ren X., Li Z., Cai Y.-F., Er X., 2024, Exploring $f(T)$ Gravity via strongly lensed fast radio bursts, [doi:10.48550/arXiv.2401.05464](https://arxiv.org/abs/10.48550/arXiv.2401.05464)
- Joyce A., Jain B., Khoury J., Trodden M., 2015, *Phys. Rep.*, 568, 1
- Khoury J., Weltman A., 2004a, *Phys. Rev. D*, 69, 044026
- Khoury J., Weltman A., 2004b, *Phys. Rev. Lett.*, 93, 171104
- Khyrkin I. S., et al., 2024, *ApJ*, 973, 151
- Kilbinger M., 2015, *Rep. Prog. Phys.*, 78, 086901
- Kilbinger M., et al., 2017, *MNRAS*, 472, 2126
- Kobayashi T., 2019, *Rep. Prog. Phys.*, 82, 086901
- Kovacs T. O., Mao, Sui Ann Basu, Aritra Ma, Yik Ki Pakmor, Ruediger Spitler, Laura G. Walker, Charles R. H. 2024, *A&A*, 690, A47
- Kumar P., Day C. K., Shannon R. M., Bhandari S., Qiu H., 2021, Transient Name Server Fast Radio Bursts, 2275, 1
- LIGO Scientific Collaboration et al., 2015, *Classical Quant. Grav.*, 32, 074001
- Lange J. U., 2023, *MNRAS*, 525, 3181
- Laureijs R., et al., 2011, Euclid Definition Study Report, [doi:10.48550/arXiv.1110.3193](https://arxiv.org/abs/10.48550/arXiv.1110.3193)
- Leistedt B., Peiris H. V., Mortlock D. J., Benoit-Lévy A., Pontzen A., 2013, *MNRAS*, 435, 1857
- Limber D. N., 1954, *ApJ*, 119, 655
- Linder E. V., 2017, *Phys. Rev. D*, 95, 023518
- Lorimer D. R., Bailes M., McLaughlin M. A., Narkevic D. J., Crawford F., 2007, *Science*, 318, 777
- Ma C.-P., Bertschinger E., 1995, *Astrophys. J.*, 455, 7
- Macquart J.-P., et al., 2020, *Nature*, 581, 391
- Masui K. W., Sigurdson K., 2015, *Phys. Rev. Lett.*, 115, 121301
- Mead A. J., Peacock J. A., Heymans C., Joudaki S., Heavens A. F., 2015, *MNRAS*, 454, 1958
- Mead A. J., Tröster T., Heymans C., Van Waerbeke L., McCarthy I. G., 2020, *Astron. Astrophys.*, 641, A130
- Mo J.-F., Zhu W., Wang Y., Tang L., Feng L.-L., 2022, *MNRAS*, 518, 539
- Muñoz J. B., Loeb A., 2018, *Phys. Rev. D*, 98, 103518
- Nicola A., García-García C., Alonso D., Dunkley J., Ferreira P. G., Slosar A., Spergel D. N., 2021, *J. Cosmology Astropart. Phys.*, 2021, 067
- Noller J., 2020, *Phys. Rev. D*, 101, 063524
- Petroff E., Hessels J. W. T., Lorimer D. R., 2019, *Astron. Astrophys. Rev.*, 27, 4
- Planck Collaboration et al., 2016, *A&A*, 594, A14
- Planck Collaboration et al., 2020a, *A&A*, 641, A1
- Planck Collaboration et al., 2020b, *A&A*, 641, A6
- Prochaska J. X., et al., 2019, *Science*, 366, 231
- Rafiei-Ravandi M., et al., 2021, *ApJ*, 922, 42
- Ratra B., 1988, *Phys. Rev. D*, 38, 2399
- Ratra B., Peebles P. J. E., 1988, *Phys. Rev. D*, 37, 3406
- Ravi V., et al., 2019, *Nature*, 572, 352
- Reischke R., Hagstotz S., 2023a, *MNRAS*, 523, 6264
- Reischke R., Hagstotz S., 2023b, *MNRAS*, 524, 2237
- Reischke R., Mancini A. S., Schäfer B. M., Merkel P. M., 2019, *MNRAS*, 482, 3274
- Reischke R., Hagstotz S., Lilow R., 2021, *Phys. Rev. D*, 103, 023517
- Reischke R., Hagstotz S., Lilow R., 2022, *MNRAS*, 512, 285
- Reischke R., Neumann D., Bertmann K. A., Hagstotz S., Hildebrandt H., 2023, Calibrating baryonic feedback with weak lensing and fast radio bursts, [doi:10.48550/arXiv.2309.09766](https://arxiv.org/abs/10.48550/arXiv.2309.09766)
- Reischke R., Kovač M., Nicola A., Hagstotz S., Schneider A., 2024, An analytical model for the dispersion measure of Fast Radio Burst host galaxies, [doi:10.48550/arXiv.2411.17682](https://arxiv.org/abs/10.48550/arXiv.2411.17682)
- Riess A. G., Filippenko A. V., Challis P., et al. 1998, *AJ*, 116, 1009
- Sawicki I., Bellini E., 2015, *Phys. Rev. D*, 92, 084061
- Secco L. F., et al., 2022, *Phys. Rev. D*, 105, 023515
- Shannon R. M., Kumar P., Bhandari S., Macquart J. P., 2019, *The Astronomer's Telegram*, 13166, 1
- Sherman M. B., et al., 2024, *ApJ*, 964, 131
- Shirasaki M., Kashiya K., Yoshida N., 2017, *Phys. Rev. D*, 95, 083012
- Shull J. M., Smith B. D., Danforth C. W., 2012, *ApJ*, 759, 23
- Spitler L. G., et al., 2016, *Nature*, 531, 202

- Spurio Mancini A., Taylor P. L., Reischke R., Kitching T., Pettorino V., Schäfer B. M., Zieser B., Merkel P. M., 2018a, *Phys. Rev. D*, 98, 103507
- Spurio Mancini A., Reischke R., Pettorino V., Schäfer B. M., Zumalacárregui M., 2018b, *MNRAS*, 480, 3725
- Spurio Mancini A., et al., 2019, *MNRAS*, 490, 2155
- Spurio Mancini A., Piras D., Alsing J., Joachimi B., Hobson M. P., 2022, *MNRAS*, 511, 1771
- Takahashi R., Ioka K., Mori A., Funahashi K., 2021, *MNRAS*, 502, 2615
- Tang L., Lin H.-N., Li X., 2023, *Chinese Physics C*, 47, 085105
- Tanidis K., Camera S., 2019, *MNRAS*, 489, 3385
- Tegmark M., Taylor A. N., Heavens A. F., 1997, *ApJ*, 480, 22
- Tiesinga E., Mohr P. J., Newell D. B., Taylor B. N., 2021, *Rev. Mod. Phys.*, 93, 025010
- Tripathi A., Sangwan A., Jassal H., 2017, *J. Cosmology Astropart. Phys.*, 2017, 012
- Tröster T., et al., 2022, *A&A*, 660, A27
- Vainshtein A. I., 1972, *Physics Letters B*, 39, 393
- Vanderlinde K., et al., 2019, The Canadian Hydrogen Observatory and Radio- transient Detector (CHORD), [doi:10.5281/zenodo.3765414](https://doi.org/10.5281/zenodo.3765414)
- Walters A., Weltman A., Gaensler B. M., Ma Y.-Z., Witzemann A., 2018, *ApJ*, 856, 65
- Weinberg D. H., Mortonson M. J., Eisenstein D. J., Hirata C., Riess A. G., Rozo E., 2013, *Phys. Rep.*, 530, 87
- Wojtak R., Hansen S. H., Hjorth J., 2011, *Nature*, 477, 567
- Wu Q., Zhang G.-Q., Wang F.-Y., 2022, *MNRAS*, 515, L1
- Xu J., et al., 2023, *Universe*, 9
- Yamasaki S., Totani T., 2020, *ApJ*, 888, 105
- Yang Y.-P., Zhang B., 2016, *ApJL*, 830, L31
- Yao J. M., Manchester R. N., Wang N., 2017, *ApJ*, 835, 29
- Zhang G. Q., Yu H., He J. H., Wang F. Y., 2020, *ApJ*, 900, 170
- Zhang X., et al., 2024, The BINGO/ABDUS Project: Forecast for cosmological parameter from a mock Fast Radio Bursts survey, [doi:10.48550/arXiv.2411.17516](https://doi.org/10.48550/arXiv.2411.17516)
- Zhou B., Li X., Wang T., Fan Y.-Z., Wei D.-M., 2014, *Phys. Rev. D*, 89, 107303
- Zumalacárregui M., Bellini E., Sawicki I., Lesgourgues J., Ferreira P. G., 2017, *J. Cosmology Astropart. Phys.*, 2017, 019

APPENDIX

A. ADDITIONAL CONSTRAINTS FROM PLANCK CMB

We additionally investigate the influence of adding information from the PLANCK2018 (Planck Collaboration et al. 2020a) temperature anisotropy power spectrum. Based on the chosen $\propto \Omega_\Lambda$ parametrisation used for modified gravity, we expect the main constraining power thereof to originate from degeneracy breaking between cosmological parameters. The posteriors are obtained by sampling the combined PLANCK2018-TT+Euclid-CS×FRB likelihood, whereas the Planck covariance is obtained from inverting the corresponding Fisher matrix and marginalising over nuisance parameters not included in the Euclid-CS×FRB likelihood.

Assuming weak modified gravity with $\hat{\alpha}_B^{\text{fid}} = \hat{\alpha}_M^{\text{fid}} = 0.05$

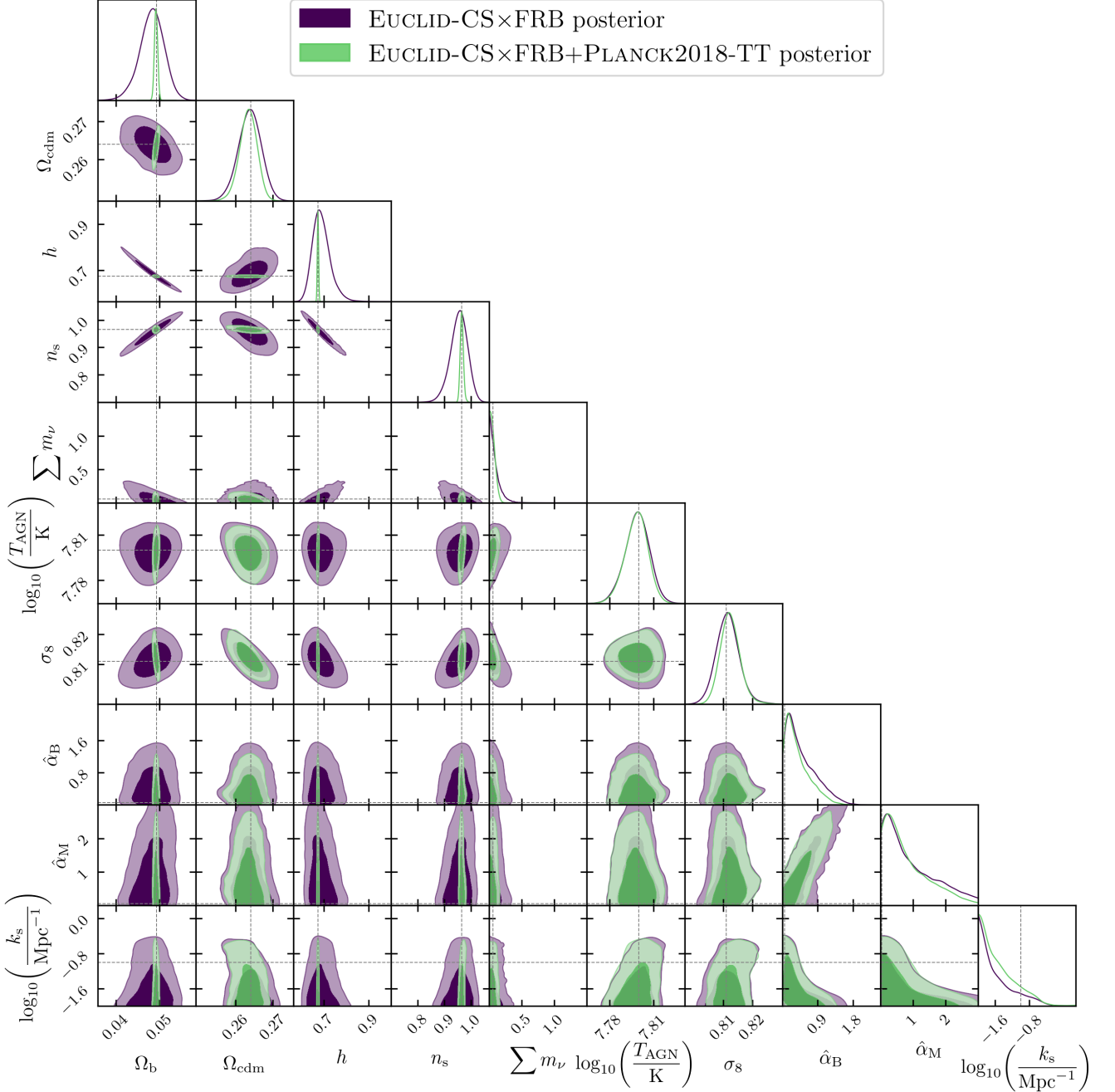


Figure A.1. 68% and 95 % posterior confidence regions (dark and light areas, respectively) for EUCLID-CS×FRB cross-correlation alone and in combination with PLANCK2018 temperature anisotropy auto-correlation. The fiducial cosmology taken from Tab. 2 is indicated by grey, dashed lines.

Furthermore, the Planck likelihood carries no information about the Horndeski screening scale and the baryonic feedback strength, hence we extend the Fisher matrix for $\log_{10}\left(\frac{T_{\text{AGN}}}{\text{K}}\right)$ and $\log_{10}\left(\frac{k_s}{\text{Mpc}^{-1}}\right)$ with small values (10^{-5}) along the corresponding diagonal, thus implying no intrinsic constraining power on these parameters. The posterior

contours for the weak modified gravity case are shown in Fig. A.1. While there is a substantial increase in constraining power on Ω_b , the 68% confidence region for h , and n_s , the $\hat{\alpha}_B$ ($\hat{\alpha}_M$) decreases only by a factor of 1.25 (1.17). The effect is even less for the strong modified gravity case, where the error margin decreases by a factor of 1.01 (1.04) for $\hat{\alpha}_B$ ($\hat{\alpha}_M$). Therefore, adding CMB temperature fluctuation information has only diminishing returns regarding modified gravity.

B. ACCURACY AND DETAILS OF THE COSMOPOWER EMULATOR

For the emulator training, we use five learning steps with subsequent learning rates of 10^{-2} , 10^{-3} , 10^{-4} , 10^{-5} , 10^{-6} . For each, the number of epochs range from a minimum of 100 for early stopping due to lack of model improvement to a maximum of 1000. Ten per cent of the data is used for validation. The batch sizes and hidden layer neuron structure for all models are depicted in Tab. 4. An analysis of the test data reveals the emulators to

model	batch sizes	hidden neuron structure
$P_{\text{mm}}(k)$	256	200×200
$b_e(k)$	256	200×200
$\eta(k)$	512	200×200
$\mu(k)$	512	200×200
$\chi(z)$	512	30×70

Table 4. *cosmopower* Emulator training settings for the $\{P_{\text{mm}}(k), b_e(k), \eta(k), \mu(k), \chi(z)\}$ models.

be accurate within 5% (see Fig. B.2 for more information).

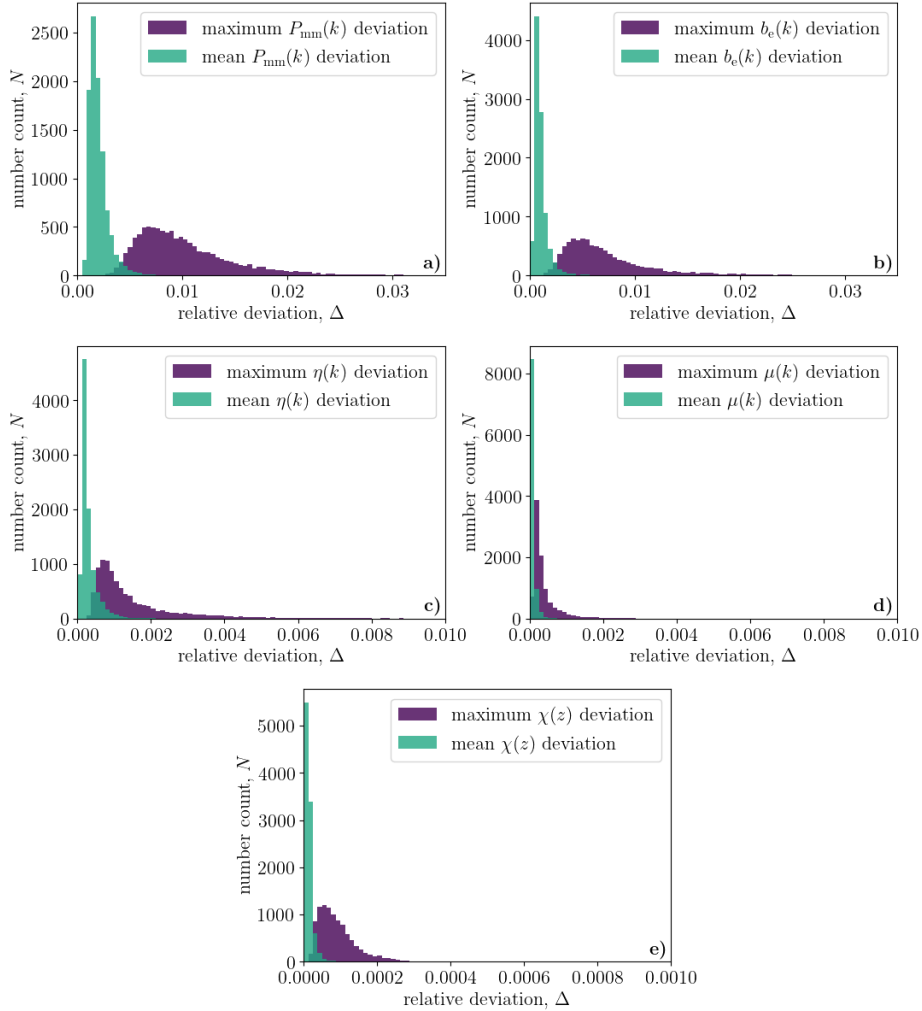


Figure B.2. Histogram of the maximum and mean deviation of the emulated a) $P_{\text{mm}}(k)$, b) $b_e(k)$, c) $\eta(k)$, d) $\mu(k)$, e) $\chi(z)$ to the simulated test data.

We use 9793 samples to test the accuracy of the emulator. To evaluate the trained neural networks, the five functions $f_i \in \{P_{\text{mm}}(k), b_e(k), \eta(k), \mu(k), \chi(z)\}$ are emulated with the same cosmological parameters used for calculating the test data set. Then, the relative deviation to the validation data is calculated as

$$\Delta := \left| 1 - \frac{f_i^{\text{cosmopower}}}{f_i^{\text{hi_class}}} \right| \quad (\text{B1})$$

for each mode, k or z , depending on the function. Finally, by taking a histogram of the maximum and mean over all modes for each set of input parameters, a visual representation of how the neural network performs at worst and on average is created, shown in Fig. B.2. At worst, the emulator deviates $\leq 3\%$ and performs much better most of the time. Therefore, we exclude the emulator as a dominating systematic in this work.

C. MCMC CONVERGENCE TEST

The convergence tests are conducted by varying the hyperparameters of Nautilus-sampler: the maximum fraction of the evidence contained in the live set before the exploration phase ends, “f_live”, and the minimum demanded effective sample size, “n_eff”. In Fig C.1 we show the results for the EUCLID-CS auto-correlations MCMCs with the fiducial cosmology given in Tab 2. Note that varying the hyperparameters has very little effect on the resulting contours, hence we use the Nautilus standard settings. Similar behaviour is obtained when testing the Euclid-CS \times FRB cross-correlation posterior for convergence.

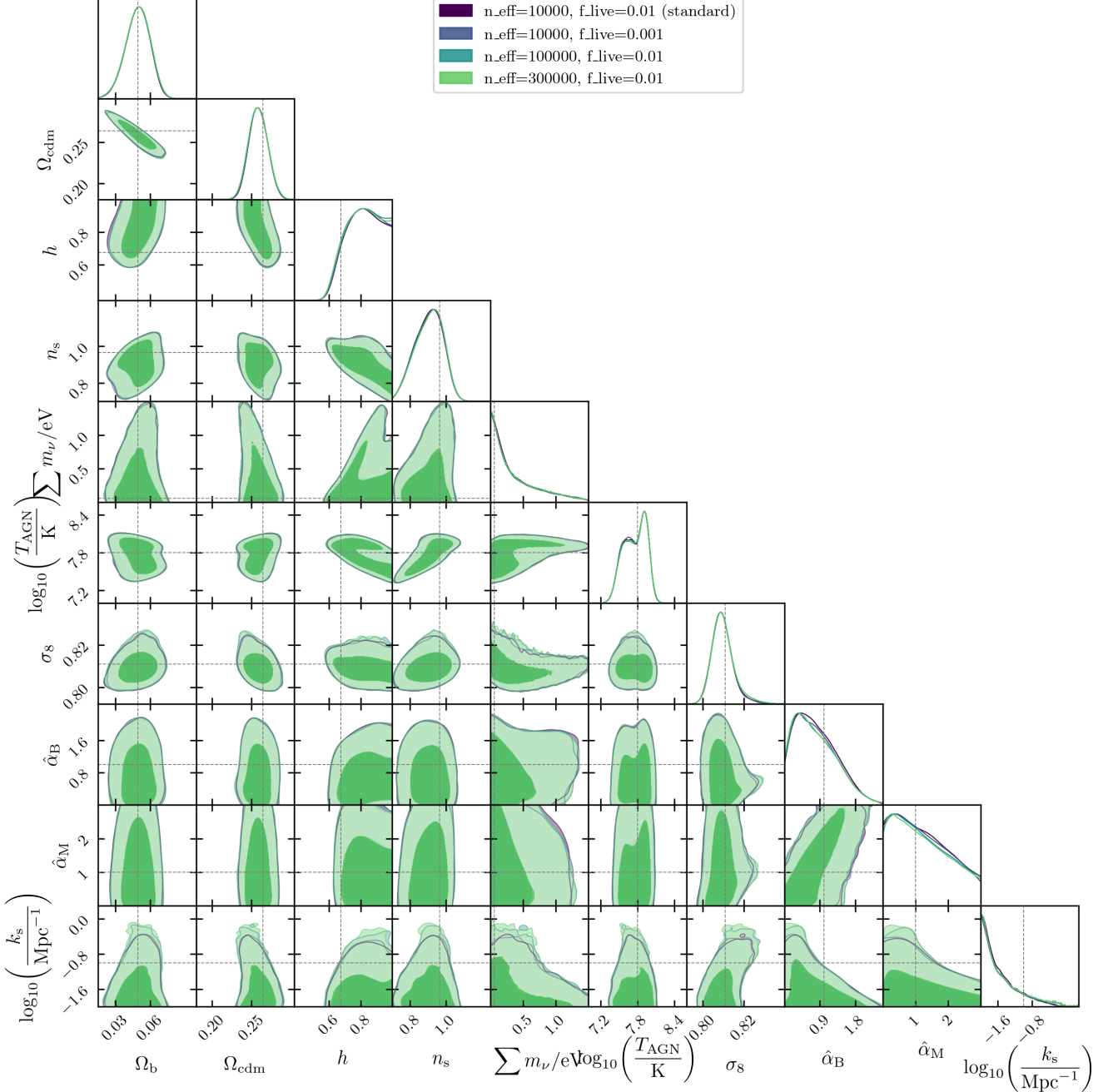


Figure C.1. EUCLID-CS auto-correlation posterior contours for different settings of Nautilus-sampler.

D. FRBS USED FOR REAL LIFE APPLICATION

In Tab. 5 we summarise all the FRBs used in Section 5:

FRB	DM _{obs}	z	DM _{MW}	ra[rad]	dec[rad]	Source
20220207C	262.38	0.04304	79.3	-2.7807	1.272	Sherman et al. (2024)
20220307B	499.27	0.248123	135.7	-2.7333	1.26	Sherman et al. (2024)
20220310F	462.24	0.477958	45.4	-2.9848	1.2827	Sherman et al. (2024)
20220418A	623.25	0.622	37.6	-2.8867	1.2234	Sherman et al. (2024)
20220506D	396.97	0.30039	89.1	-2.7715	1.2711	Sherman et al. (2024)
20220825A	651.24	0.241397	79.7	-2.7786	1.2668	Sherman et al. (2024)
20220920A	314.99	0.158239	40.3	-2.862	1.2378	Sherman et al. (2024)
20221012A	441.08	0.284669	54.4	-2.8149	1.2309	Sherman et al. (2024)
20220914A	631.29	0.1139	47.55	1.7812	1.28	Sherman et al. (2024)
20220509G	269.53	0.0894	46.55	1.7919	1.226	Sherman et al. (2024)
20190608A	339.5	0.1178	204.75	2.6882	-0.1378	CHIME/FRB Collaboration et al. (2021)
20200430A	380.1	0.1608	112.21	0.8675	0.216	Kumar et al. (2021)
20150517A	560.0	0.19273	37.53	-1.6929	0.5783	Spitler et al. (2016)
20191001A	506.92	0.234	24.87	2.502	-0.9555	Shannon et al. (2019)
20190714A	504.7	0.2365	154.47	0.0695	-0.2273	Bhandari et al. (2019)
20190102C	363.6	0.291	17.67	2.4856	-1.3871	Macquart et al. (2020)
20180924B	362.4	0.3212	34.43	2.55	-0.7138	Bannister et al. (2019)
20200906A	577.8	0.3688	91.27	-2.2079	-0.2458	Bhandari et al. (2022)
20190611B	321.4	0.378	17.76	2.4565	-1.3857	Macquart et al. (2020)
20181112A	589.27	0.4755	25.76	2.5717	-0.9245	Prochaska et al. (2019)
20190523A	760.8	0.66	18.76	0.4724	1.2648	Ravi et al. (2019)

Table 5. FRBs used for the analysis presented in Section 5.